THE ASTROPHYSICAL JOURNAL, 454:623–642, 1995 December 1

THE CENTRAL REGION IN M100: OBSERVATIONS AND MODELING

J. H. KNAPEN,[1,2] J. E. BECKMAN,[2,3] C. H. HELLER,[4,5] I. SHLOSMAN,[4,6,7] AND R. S. DE JONG[8,9]

Received 1994 November 4; accepted 1995 June 12

ABSTRACT

We present new high-resolution observations of the central region in the late-type spiral galaxy M100 (NGC 4321) supplemented by three-dimensional numerical modeling of stellar and gas dynamics, including star formation (SF). Near-infrared imaging has revealed a small bulge of 4″ effective diameter; a 60″ radial length stellar bar of moderate strength, previously inferred from optical and 21 cm observations; and an ovally shaped, ringlike structure in the plane of the disk between 10″–22″ from the center, whose major axis makes a large angle with the bar. The K isophotes become progressively elongated and skewed to the position angle of the bar *both* outside and inside the "ring," forming an inner barlike region. The galaxy exhibits a mild circumnuclear starburst concentrated in the inner part of the K "ring." This SF is prominent in Hα and the U, B, and V bands, forming an incomplete ring. In addition, two strong local maxima of K emission have been observed to lie remarkably symmetrically with respect to the galactic nucleus and equidistant from it at 7″.5, slightly leading the stellar bar. CO molecular emission is peaked in the dust lanes seen in the $I-K$ color index image.

We interpret the twists in K isophotes and the swinging of spiral arms through $\sim 360°$ inside the corotation radius as being indicative of the presence of a double inner Lindblad resonance (ILR) and test this hypothesis by modeling the gas flow in a self-consistent gas+stars disk embedded in a halo, with an overall NGC 4321–like mass distribution in the system. Both ILRs have been verified using nonlinear orbit analysis by determining the spatial extent of the family of orbits oriented along the minor axis of the bar.

We have reproduced the basic morphology of the region inside corotation, including (1) the $\sim 60''$ bar; (2) the large-scale trailing shocks representing the offset dust lanes in the bar; (3) two symmetric K peaks corresponding to gas compression maxima which lie at the caustic formed by the interaction of a pair of trailing and leading shocks in the vicinity of the inner ILR, both peaks being sites of SF; and (4) two additional zones of SF corresponding to gas compression maxima at the bar's minor axis, where the large-scale shocks start to curl and which are referred in the literature as "twin peaks." We argue further that the twisting of K isophotes in the neighborhood of the resonance region requires a population of red stars which are dynamically young and follow gas rather than stellar orbits, i.e., red supergiants. At the same time, a substantial contribution from OB stars to the K light is expected within the inner kiloparsec and especially in the symmetric K peaks. We also conclude that NGC 4321 hosts a single stellar bar which fuels the starburst activity within the circumnuclear "ring" by channeling gas there at the median rate of ~ 0.1–$1\ M_\odot\ \mathrm{yr}^{-1}$.

Subject headings: galaxies: evolution — galaxies: individual (NGC 4321 = M100) — galaxies: kinematics and dynamics — galaxies: nuclei — galaxies: photometry — galaxies: spiral — galaxies: starburst — galaxies: structure

1. INTRODUCTION

The central regions of disk galaxies are frequent sites of enhanced activity, most probably fueled by the inflow of galactic interstellar medium (hereafter ISM). Known manifestations, Seyfert nuclei and nuclear starbursts, differ substantially in their physical nature and activity level, which in most cases cannot be maintained for periods much longer than $\sim 10^8$ yr without some refueling mechanism (e.g., reviews by Begelman, Blandford, & Rees 1984; Telesco 1988; Heckman 1990; Shlosman, Begelman, & Frank 1990; Athanassoula 1994; and references therein). This must entail a means of resupplying gas used up in stars and lost in galactic superwinds driven by nuclear starbursts, or accreted by central black holes (BHs) in active galactic nuclei (AGNs).

The problem of driving the gas into the center of a disk galaxy is that of shedding angular momentum in a rotating system. On galactic scales, ~ 1–10 kpc, this can be achieved by means of gravitational torques from nonaxisymmetric features such as stellar bars, oval distortions, and spiral arms, as suggested originally by Simkin, Su, & Schwarz (1980). Gravitational torques result in a catastrophic loss of angular momentum by the ISM; the efficiency of this process depends on the particular perturbation and its amplitude. The gas-dynamical processes become increasingly important on scales $\lesssim 1$ kpc, as noted by Shlosman, Frank, & Begelman (1988, 1989) and Heller & Shlosman (1994), where (1) the gas gravity can affect the stellar dynamics, inflow rates, and star formation

[1] Département de Physique, Université de Montréal, C.P. 6128, Succursale Centre Ville, Montréal, QC H3C 3J7, Canada, and Observatoire du Mont Mégantic; knapen@astro.umontreal.ca.
[2] Instituto de Astrofísica de Canarias, E-38200 La Laguna, Tenerife, Spain.
[3] jeb@iac.es.
[4] Department of Physics and Astronomy, University of Kentucky, Lexington, KY 40506-0055.
[5] Present address: Universitäts Sternwarte Göttingen, 11 Geismarlandstrasse, 37083 Göttingen, Germany; heller@uni-sw.gwdg.de.
[6] Gauss Foundation Fellow, Academy of Sciences, Göttingen, Germany.
[7] shlosman@asta.pa.uky.edu.
[8] University of Durham Department of Physics, South Road, Durham DH1 3LE, England, UK; R.S.deJong@durham.ac.uk.
[9] Kapteyn Astronomical Institute, Postbus 800, NL-9700 AV Groningen, the Netherlands; roelof@astro.rug.nl.

(SF); (2) inner Lindblad resonances (ILRs) between a stellar disk and a bar, if present, are expected to be found; and (3) a radial inflow should slow down in the neighborhood of ILRs (or the Q-barrier, where Q is Toomre's [1964] parameter), and the resulting accumulation of gas may serve as a precursor of a nuclear starburst. Finally, deep within the potential well and a few parsecs from the BHs in AGNs, an angular momentum transport may be dominated by magnetic torques (Blandford & Payne 1982; Emmering, Blandford, & Shlosman 1992).

Departure from axisymmetry on the galactic scale may be very explicit in some cases: e.g., about half the observed disk galaxies are barred (e.g., de Vaucouleurs 1963; Sellwood & Wilkinson 1993, and references therein), or less evident in other: many galactic disks are ovally distorted, which is clear both on kinematic (Bosma 1981) and photometric (Kormendy 1982) grounds and some bulges are triaxial (Norman & Silk 1983; Pfenniger & Norman 1990; Kormendy 1993). In fact, as more near-infrared (NIR) images of galaxies become available, an increasing number of galaxies are seen to have major distortions and bars in their stellar mass distribution (e.g., Hackwell & Schweizer 1983; Scoville et al. 1988; Thronson et al. 1989; Telesco et al. 1991; Zaritsky, Rix, & Rieke 1993; Block et al. 1994). Thus, the basic dynamical precondition for sustained circumnuclear activity at some level appears to exist in the majority of disks. On the other hand, observational evidence supporting the recent redistribution of the ISM on galactic scale and correlation of central activity with the presence of nonaxisymmetric features is growing (Lo et al. 1987; Nakai et al. 1987; Ishizuki et al. 1990; Meixner et al. 1990; Taniguchi et al. 1990; Wang, Scoville, & Sanders 1991; Kenney et al. 1992; Martin & Roy 1994; Scoville et al. 1994; Moles, Márquez, & Pérez 1995).

Central starburst activity is enhanced in barred spirals, as evidenced from optical, Hα, radio, and infrared (IR) surveys (Adams 1977; Simkin et al. 1980; Hummel 1981; Balzano 1983; Devereux 1987; Puxley, Hawarden, & Mountain 1988; Telesco, Dressel, & Wolstencroft 1993; see also review by Kennicutt 1994, and references therein). It often delineates (roughly) kiloparsec-size ringlike structures of SF regions mixed with dust, called nuclear rings. At superior resolution, these "rings" may consist of tightly wound spiral arms and be patchy and incomplete (e.g., Pogge 1989; Buta & Crocker 1993). Rings have been detected in UV, optical, NIR, and radio continua, as well as in Hα and CO, and they are associated with the ongoing SF. In early-type galaxies, S0/a–Sab, the SF activity, as manifested by bright H II regions, is almost entirely limited to these rings (e.g. Pogge 1989; Dressel & Gallagher 1994). In late-type spirals, the nuclear rings also stand out, as a result of their high surface brightness.

The position and morphology of nuclear "rings" may be related directly to the large-scale dynamics in disk galaxies for which they in fact serve as probes. In particular, they seem to be associated with the ILRs of barred stellar disks and as such impose constraints on the bar pattern speed and on the possible gas flow (e.g., Telesco & Decher 1988; Kenney et al. 1992; Athanassoula 1994). Moreover, nuclear "rings" correlate with the presence of leading dust lanes, which themselves delineate offset shocks in the stellar bar (Prendergast 1962; Athanassoula 1992). Properties of nuclear "rings" have been studied in a number of works, observationally (Buta 1986a, b; Buta & Crocker 1993; Shaw et al. 1993; and others) and theoretically (Schwarz 1984; Combes & Gerin 1985; Athanassoula 1992; Elmegreen 1994; Heller & Shlosman 1995). Their intrinsic shapes vary from circular to moderately elliptical, and they lead the stellar bars typically by $\sim 50°$–$90°$.

The galaxy M100 (NGC 4321), the brightest spiral in the Virgo Cluster, has been known to exhibit mild SF activity in the circumnuclear region since the work of Morgan (1958) and its inclusion in the Sérsic & Pastoriza (1967) list of "hot spot" galaxies. The spectrum, dominated by H II regions in the "ring," changes to LINER-type when using smaller apertures, thus showing that the nucleus is probably mildly active (Kennicutt, Keel, & Blaha 1989). Classified by Sandage (1961) as Sbc, NGC 4321 is favorably inclined at $30° \pm 3°$ (de Vaucouleurs, de Vaucouleurs, & Corwin 1976, hereafter RC2; see also Knapen et al. 1993a), and its barred nature has been noted in the RC2 where it was defined as an SAB(s)bc. A pair of offset dust lanes penetrating the central region can be clearly observed in an optical photograph (Sandage & Bedke 1988). Both the stellar bar and the central oval distortion, associated with the 1 kpc ring of SF regions, have been confirmed and studied by Pierce (1986) and Arsenault et al. (1988). Pierce argued in favor of an ILR in the vicinity of the ring; Arsenault et al. based their claim of two ILRs on the Hα rotation curve. The "ring" has a distinct four-arm spiral pattern (Pogge 1989; Cepa & Beckman 1990). Knapen et al. (1993a) confirmed the few kpc bar using a broad H-band image in the NIR (shown in Fig. 5 of the present paper) and by constructing a velocity field of the 21 cm H I emission. This revealed gas flow in highly elongated orbits along the bar major axis, in accordance with hydrodynamical models (e.g., Huntley 1980; Athanassoula 1992; Friedli & Benz 1993; Heller & Shlosman 1994). Finally, Knapen et al. (1995a, hereafter Paper I) have studied optical and NIR morphologies of the central kiloparsec region at high resolution, exposing the inner barlike region. The inner barlike region was noticed also by Shaw et al. (1995), but the inferior resolution of their image as compared to ours (Paper I) led them miss crucial morphological details, such as those discussed in Paper I and below.

The galaxy has also a small companion, NGC 4322, which may be causing some distortion and asymmetry in the gas velocity and distribution of the outer disk, as picked out especially at 21 cm (Knapen et al. 1993a). In the present paper, we use the distance of $D = 13.6$ Mpc to NGC 4321 (de Vaucouleurs 1984); thus, 15″ corresponds to 1 kpc, and 1″ corresponds to 67 pc. (This distance was recently updated to 17.1 Mpc [Freedman et al. 1994], but since our numerical simulations are not scalable, we retain the old value without the loss of generality.)

This paper is devoted to observational and numerical studies of gas and stellar responses within the resonant central region of a barred disk galaxy with a particular emphasis on NGC 4321. We aim at understanding the observed morphology and its relationship to the SF processes there. The numerical part, especially that related to modeling of SF, should be viewed as providing qualitative insight into the evolution. In § 2 we present high-resolution Hα and NIR K-band photometric images of the central region in NGC 4321 supplemented with broadband optical observations. In § 3 we examine in detail the morphology of the stellar populations and that of the gas as inferred from the dust and CO distributions (the CO data were kindly provided by B. Canzian). This is followed (§ 4) by modeling numerically the evolution of the inner part of a two-component, gas + stars, self-gravitating disk whose rotation curve follows from an NGC 4321–like radial mass distribution, focusing on the formation of nuclear rings. In § 5, we

show that the observed morphology in the central kiloparsec can be explained by resonant response to the perturbing force of a moderate strength stellar bar in the presence of two ILRs. Additional comments are given in the last section.

2. OBSERVATIONS

2.1. *Optical and NIR Observations*

Broadband optical images in the *U*, *B*, *V*, *R*, and *I* Johnson photometric bands were obtained the night of 1993 May 14, at the 4.2 m William Herschel Telescope (WHT) at La Palma, using the Auxiliary focus camera at the $f/11$ Cassegrain focus of the telescope. An EEV P88300 CCD detector was used, which gives an image scale of 0.″10 per 22 μm CCD pixel, with a field of view of 2′ diameter. The images were reduced in a standard way by removing a bias level, correcting large-scale variations in sensitivity over the chip surface using dawn flat-field images, and subtracting the sky background level using sky frames taken of a nearby empty field shortly after the galaxy images. Since the exposure times were short, the number of cosmic rays on the images is small, and no attempts were made to remove them. Exposure times were 600 s for the image in the *U* band, 180 *s* for that in *B*, and 60 s for those in *V*, *R*, and *I*. Seeing values were 0.″8 $\pm$ 0.″1. FWHM. The images were taken under photometric conditions and calibrated by observing a standard star from the list of Landolt (1983).

A *K*-band image ($\lambda = 2.2$ μm; $\Delta\lambda = 0.42$ μm) was obtained by R. F. Peletier on the night of 1994 June 5 at the UK IR Telescope (UKIRT) using the IRCAM3 camera (Paper I). This camera was equipped with a 256 × 256 array, giving a pixel scale of 0.″286 and a field of view of about 70″ × 70″. Twelve separate images of the central region in NGC 4321, 60 s each, interleaved with eight exposures of the sky background, were taken. The standard data reduction procedures of bias subtraction, flat-fielding (using the night-sky frames), and averaging were applied to produce the final frame, a sum of the four separate images with best seeing. The resolution of the final image is some 0.″8. The image was calibrated by comparing it with a photometric *K*-band image obtained earlier (de Jong & van der Kruit 1994).

The images in the different photometric bands were aligned by fitting Gaussian profiles to a number of field stars in the images. We also obtained the exact resolution from these fits. This positioning was performed to a precision of better than 0.2 of a pixel, or 0.″02 (0.″05 in *K*), much better than the resolution in the images. The positions of some of the stars, as determined using the *Hubble Space Telescope* (*HST*) Guide Star Catalog, and the position of the center of the galaxy were used to place the images on a correct R.A.-declination grid, with an estimated precision of a few arcseconds. The central 40″ × 40″ areas of the images in the *U*, *B*, *V*, *R*, *I*, and *K* bands are shown in Figure 1 (Plates 31–33). A more detailed *K* image in contour representation is given in Figure 2 (Plate 34).

Color index images have been produced by dividing images in different photometric bands. To take account of the slightly different resolutions of the individual images, for each pair of images we convolved the one with the better seeing with a Gaussian to yield the resolution of the other image. The $U-I$ image, with a resolution of 0.″85 × 0.″85, is presented in Figure 3. An optical-NIR $I-K$ color index image (made after transforming the *K*-band image to an artificial grid of 0.″1 pixel^{-1}),

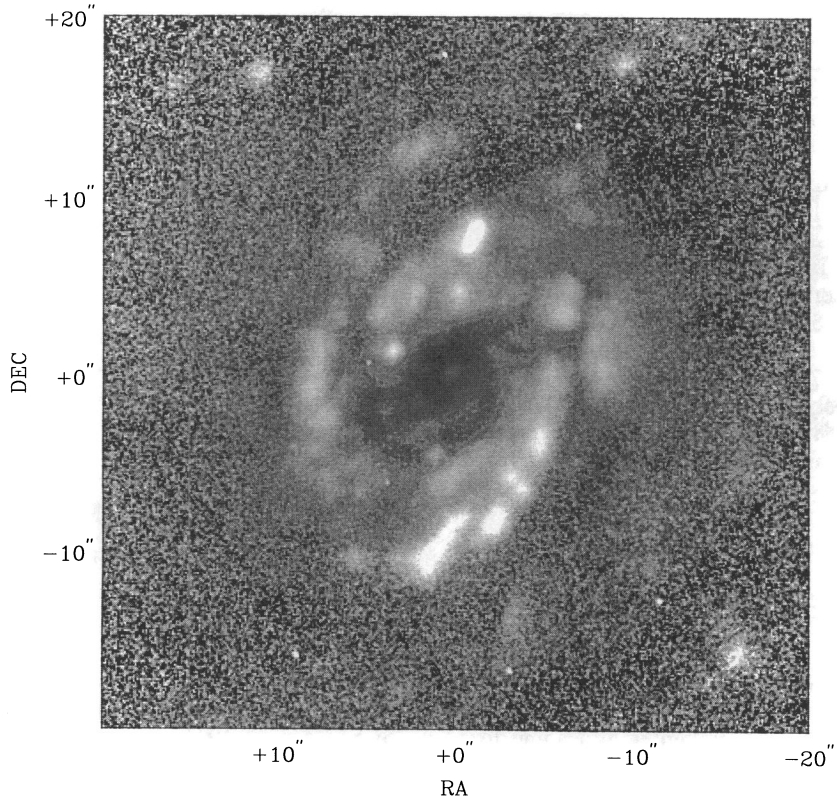

FIG. 3.—Gray-scale representation of $U-I$ color index image. Darker shades mean redder colors (relatively more *I* emission). Gray scales vary from −0.5 to 3 mag.

1995ApJ...454..623K

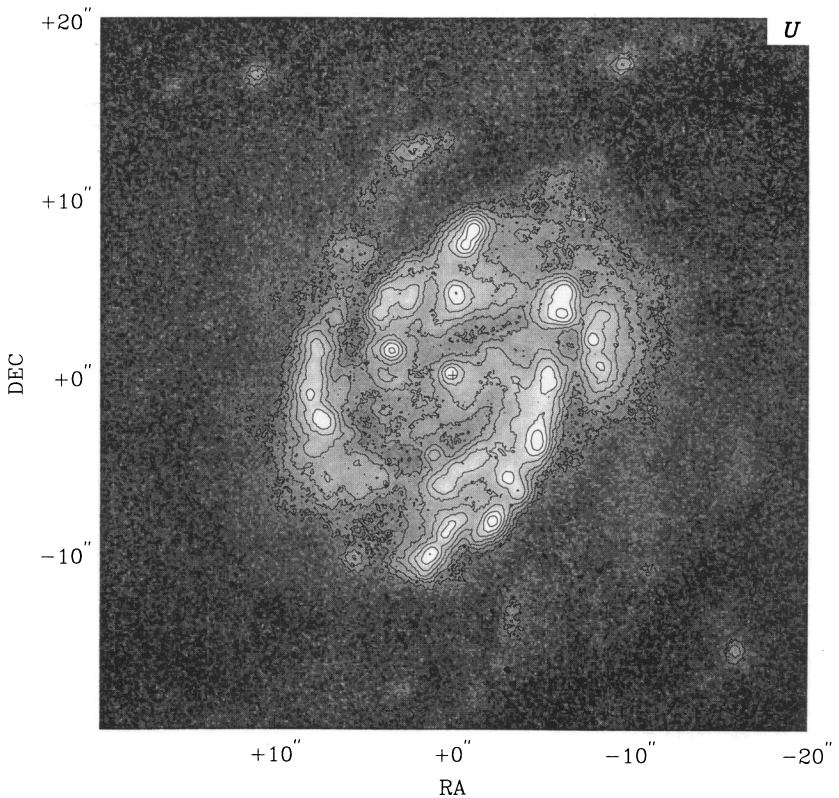

FIG. 1*a*

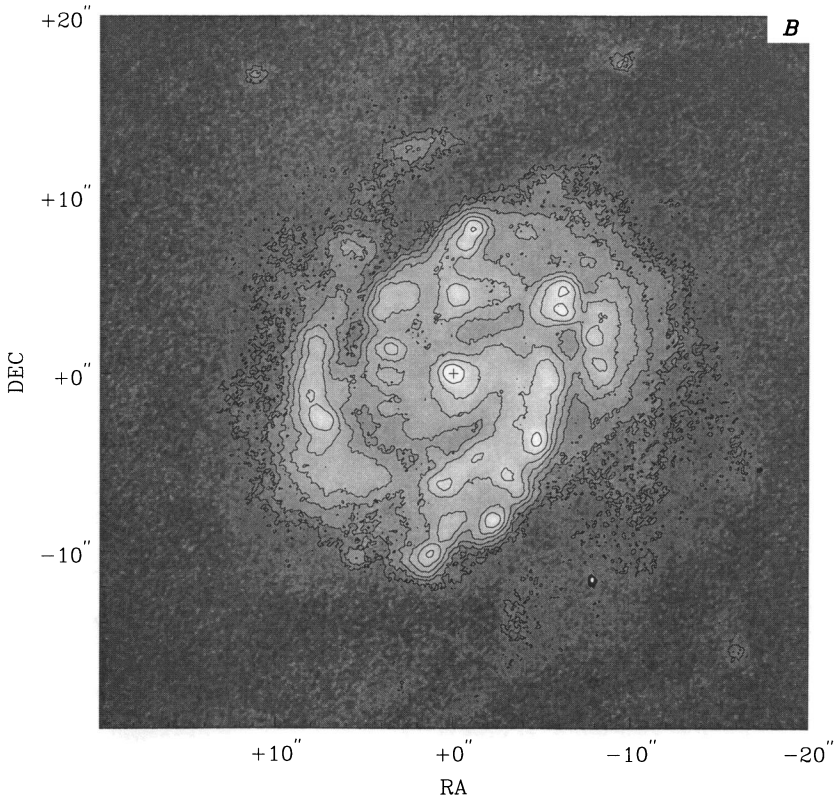

FIG. 1*b*

FIG. 1.—Panel of images of the central region in NGC 4321 in six different optical and NIR passbands: (*a*) *U*, (*b*) *B*, (*c*) *V*, (*d*) *R*, (*e*) *I*, and (*f*) *K*. Contours are shown overlain on a gray-scale representation of the same image in each panel, where darker shades represent lower intensities. Contour intervals are 0.5 mag in all panels, ranging from 20.5 to 17.5 (*U*), 21.0 to 17.5 (*B*), 20.0 to 16.5 (*V*), 19.5 to 16.0 (*R*), 19.0 to 15.0 (*I*), and 17.0 to 13.5 (*K*). The spatial resolution is 0.″8 ± 0.″05 in all panels. Area shown and scale are the same in all panels, and also in all subsequent figures, unless stated otherwise. A bright cosmic-ray hit stands out clearly toward the SW in the *B*-band image.

KNAPEN et al. (see 454, 625)

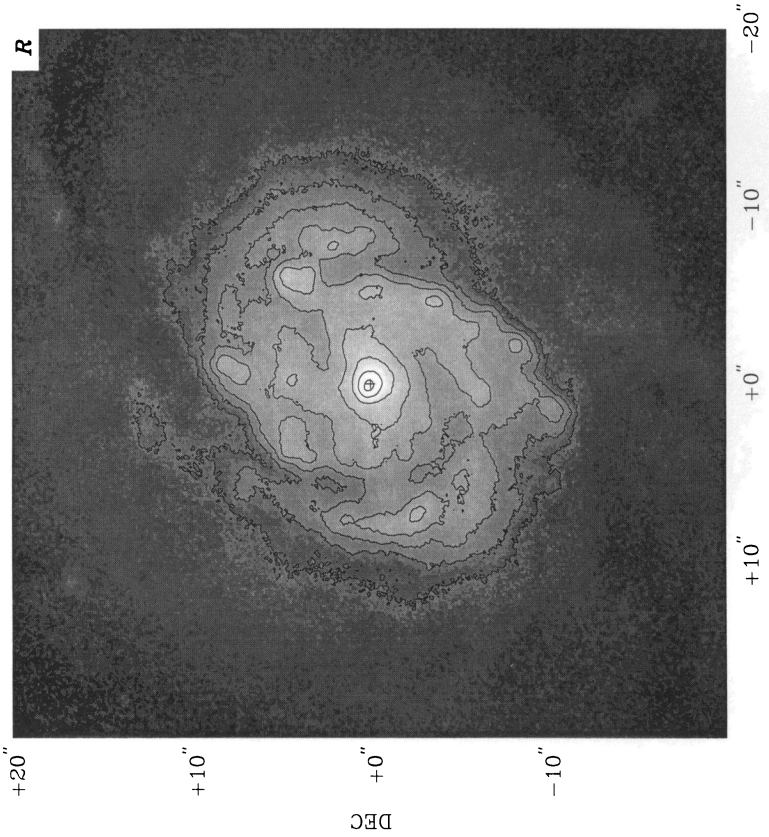

FIG. 1*d*

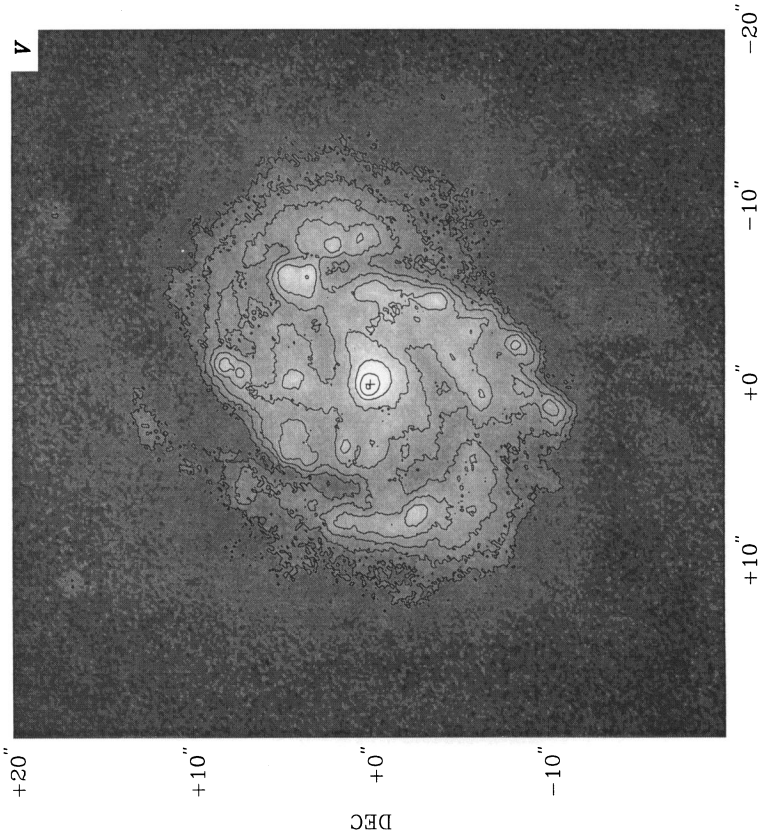

FIG. 1*c*

KNAPEN et al. (see 454, 625)

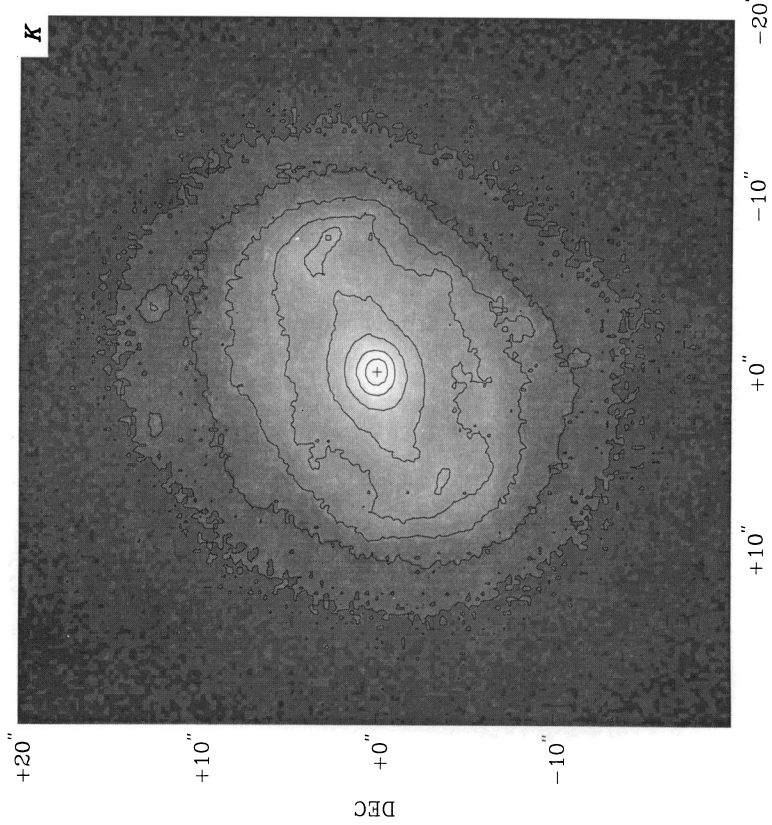

FIG. 1f

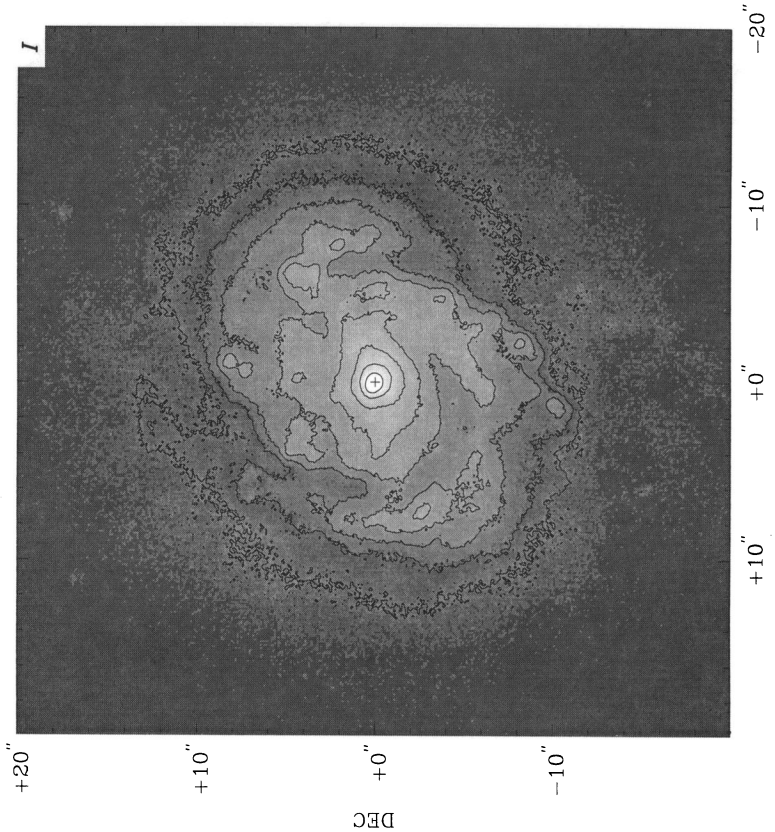

FIG. 1e

KNAPEN et al. (see 454, 625)

PLATE 34

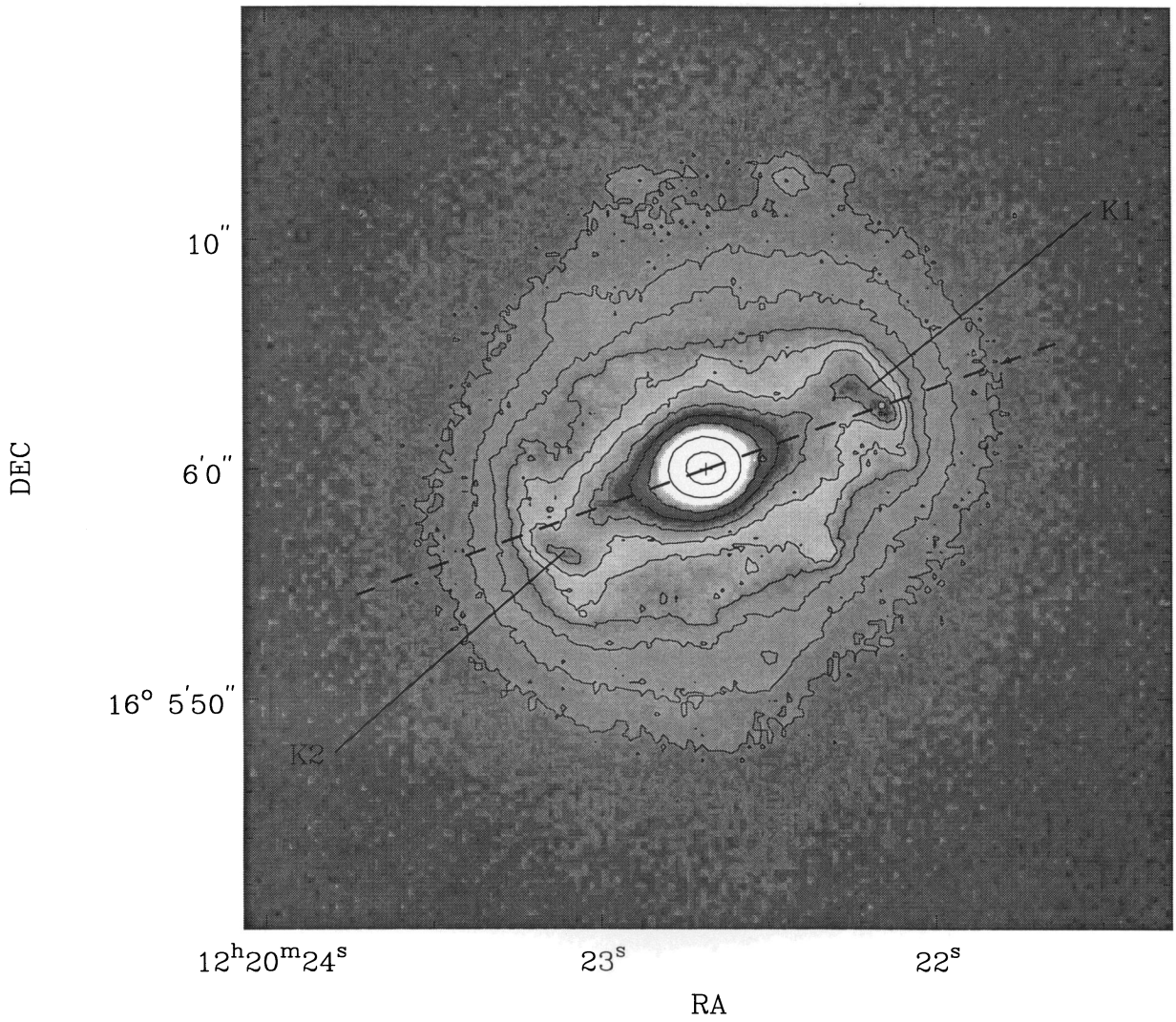

FIG. 2.—Contour representation of the NIR *K*-band image overlain on a gray-scale representation of the same image. Dashed line indicates the position angle of the *large-scale* bar (not shown in this figure), at P.A. = 107°. K1 and K2 indicate "hot spots" in *K*, further discussed in the text. Contour levels are 16.7, 16.3, 15.9, 15.6, 15.4, 15.2, 15.0, 14.8, 14.6, 14.2, 13.6, and 13.0 *K* mag.

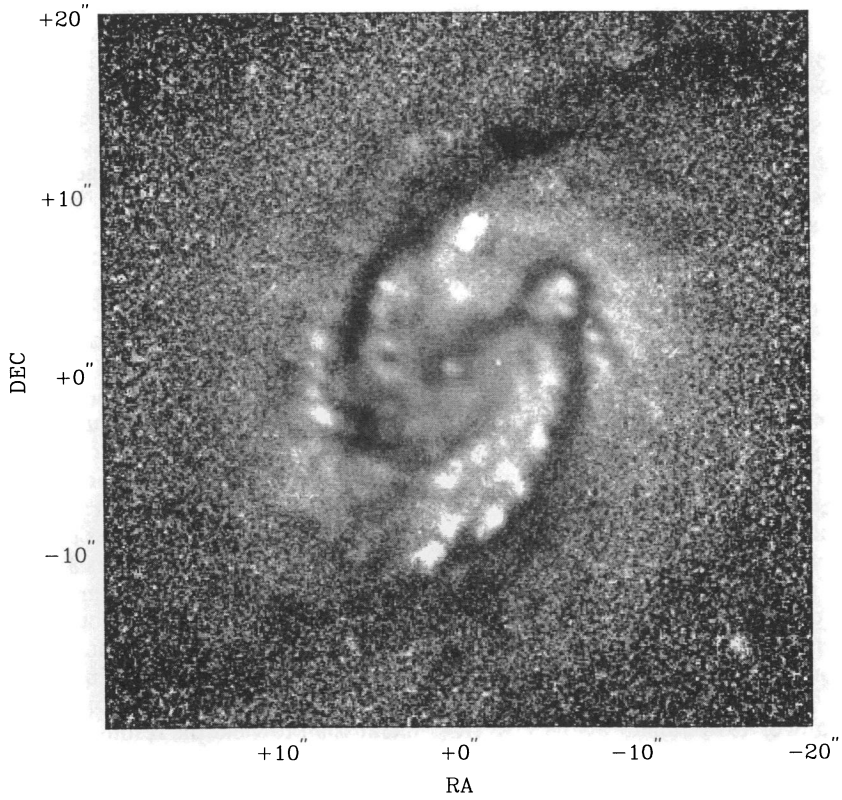

FIG. 4.—$I-K$ color index image, where darker shades indicate redder colors or relatively more K emission, which can be interpreted as higher dust extinction. Gray scales are from 1.4 (light) to 3.1 (dark) mag.

also with a resolution of some 0".8 FWHM, is shown in Figure 4.

2.2. *Narrow-Band* Hα *Observations*

The Hα line observations of NGC 4321 were made in 1991 May (eastern half of the galaxy) and 1992 March (western half) using the 4.2 m WHT with the TAURUS instrument in imaging mode, during bright and photometric sky conditions. An EEV CCD chip with pixels of projected size 0".27 × 0".27, giving a field of view (vignetted by the filter) of some 5′ diameter, was used. Redshifted 15 Å wide narrow-band interference filters were applied, both for the line (using a 6601 Å filter) and the continuum images (6577 Å and 6565 Å filters for eastern and western half, respectively). Exposure times were 1200 s for both the on-line and the continuum images of the eastern half, and 2 × 900 s for the on-line and continuum images of the western half of the galaxy.

Since the galaxy is larger than the available field of view, it was observed in four different fields, making sure the center of the galaxy was well visible in a corner of the chip. For each of these images, the basic reduction procedure (flat-fielding, positioning of the separate images, continuum subtraction, and calibration) was followed as described by Knapen et al. (1993b) for the Hα image of NGC 6814. The four continuum-subtracted Hα frames were then scaled and combined into a mosaic using positions of the galaxy center and some foreground stars seen in at least two different frames. The exact R.A.-declination orientation was determined by measuring the positions of foreground stars in the image that are listed in the *HST* Guide Star Catalog. The resulting total image covers all of the disk, up to well outside D_{25}, with a resolution (seeing FWHM) of less than 1".0 over the whole field. Its inner part is shown in Figure 5. The inset in Figure 5 was taken from the subimage that had the best resolution; seeing is ~0".8.

2.3. *Hubble Space Telescope Observations*

The *HST* was used to image the central region of NGC 4321 employing the restored WFPC. One of these images was retrieved from the HST archive: a 900 s exposure obtained on 1993 December 31 with the planetary camera through the F555W filter (roughly equivalent in wavelength to a V-band filter). A considerable number of cosmic-ray hits were removed from the image by replacing affected pixels by values interpolated from neighboring pixels. The resolution of the image as used here is considerably higher than that of all the other data. The *HST* image is shown in comparison with the K image (which is overlain in contours) in Figure 6.

2.4. CO *Interferometric Data*

For comparison with the optical and NIR data, we used a CO emission image obtained by Canzian (1990) in 1986 with the Owens Valley millimeter-wave interferometer array. The observations, calibration, and further reduction are described in detail by Canzian (1990). The 65" primary beam covers the inner region of the galaxy, and the synthesized beam in the image as used here, is 6".9 × 4".4 with a position angle (P.A.) of −3°.5. Positional accuracy is estimated to be one-fifth of the beam, or ~1". The CO contour map is shown in Figure 7, overlain on the $I-K$ color index map of Figure 4.

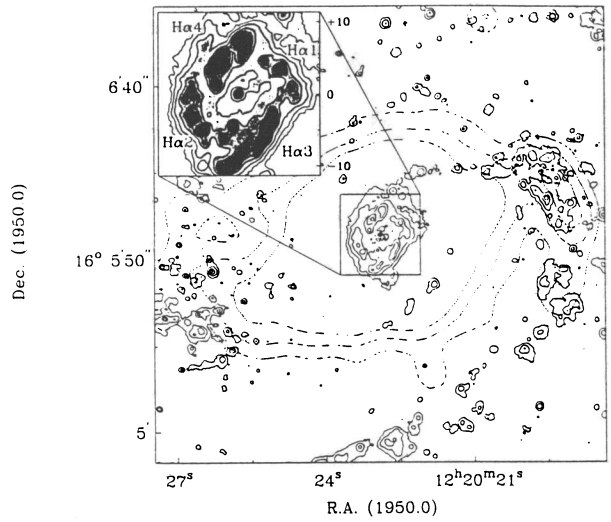

FIG. 5.—Continuum-subtracted Hα image of the central 3′ of NGC 4321 showing part of the disk which includes the 60″ large-scale bar. Effective spatial resolution is <1″. The inset shows an amplification of the circumnuclear region (labels are in arcseconds; resolution 0.″8), with emitting regions Hα1, Hα2, Hα3, and Hα4 indicated. The dotted lines are representative *H*-band contours outlining the outer large-scale bar (*H* image from Peletier & Willner 1991, kindly supplied by R. F. Peletier). Contour levels for the Hα image are 0.7, 2.1, 6.3, 12.6, and 25.2 × 10^{36} ergs s^{-1}, and (inset) 0.7, 1.4, 2.8, 5.6, 8.4, 11.2, 16.8, and 22.4 × 10^{36} ergs s^{-1}.

3. OBSERVED MORPHOLOGY

3.1. *Disk Morphology*

Understanding of the circumnuclear morphology in NGC 4321 relies on its relationship to the rest of the galaxy, which is a grand-design two-armed spiral (see Peletier 1994 for a high-quality true-color image). Elmegreen & Elmegreen (1984) classify the galaxy in their "class 12," i.e., having very well defined arms, although the asymmetry of its recent SF is less striking than that of M51 (Knapen et al. 1992, 1995b). The massive SF efficiency in the arms is some 3 times higher than in the inter-arm disk, in the rather well-defined southern arm, and also in the more flocculent northern arm (Knapen et al. 1995b). The IR-to-blue luminosity for NGC 4321 is $L_{\rm FIR(1-500\,\mu m)}/L_B = 0.42$ (Young et al. 1989), indicating that this galaxy is relatively quiet, compared to, e.g., AGN hosts or extreme starbursts. The galaxy contains a bar, of radial length 4 kpc at P.A. = 107° ± 3°, close to the P.A. found by Pierce (1986), using an *I*-band CCD image, and confirmed by Knapen et al. (1993a) using a combination of H I (21 cm) kinematics and NIR (*H*-band) photometry. This is reproduced in Figure 5, where the *H*-band isophotes are strongly elongated at the P.A. of the bar, and where clear Hα peaks are visible near its ends. Little SF is observed along the bar at smaller radii until the circumnuclear zone is reached at ~500–1400 pc from the center. Inside ~500 pc, the SF drops again (with the possible exception of the nucleus). As seen in Figure 5, the only SF associated

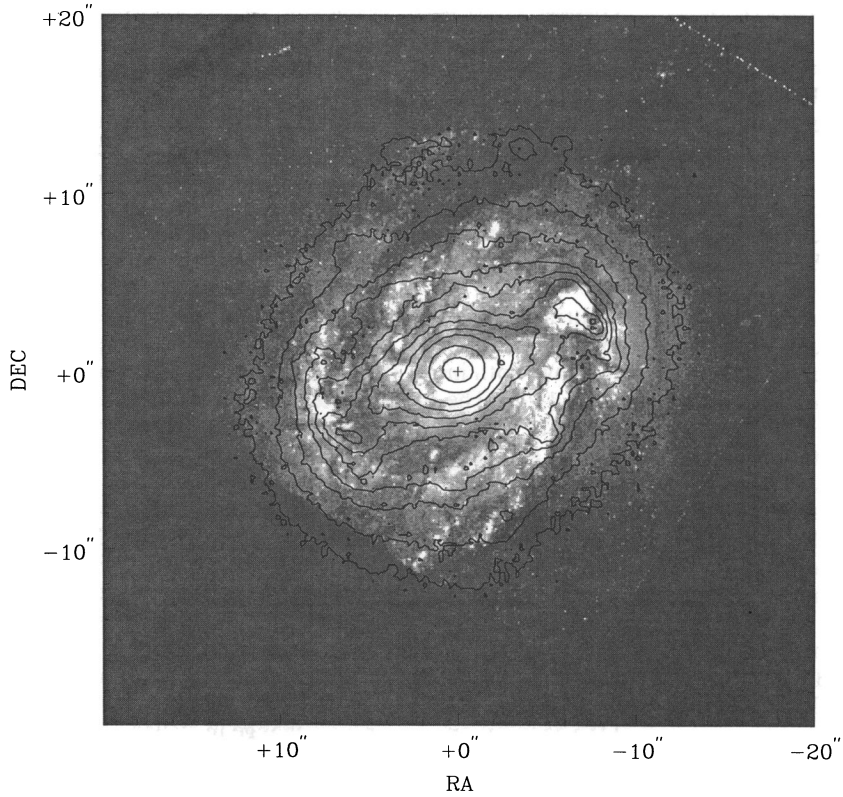

FIG. 6.—Overlay of our *K*-band image (contours as in Fig. 2) on an image in the visible taken with the *HST* (gray scales, lighter shades in the figure indicating stronger emission). The *HST* image has been degraded, but its resolution is still superior to that of the *K*-band image.

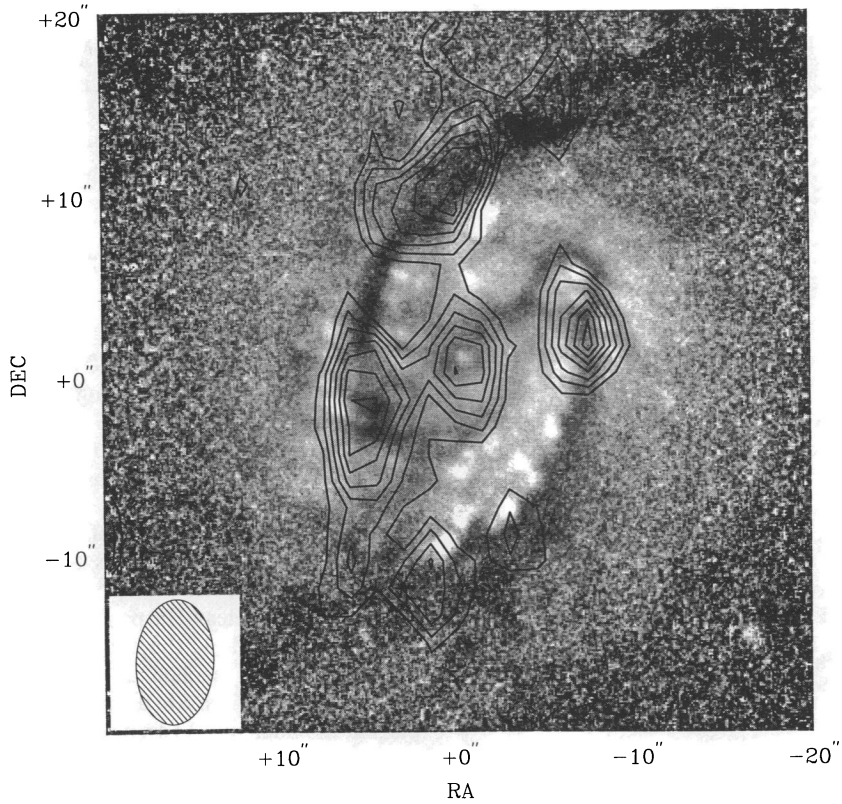

FIG. 7.—Overlay of a contour representation of an interferometric map of ^{12}CO $J = 1 \rightarrow 0$ emission (courtesy B. Canzian) on our $I-K$ color index map (*gray scales*). CO contours are at 22%, 35%, 47%, 58%, 70%, 81%, and 93% of peak intensity. $I-K$ grays range from 1.4 (light) to 3.1 mag (dark). The beam size for the CO observations is indicated. Note that all peaks seen in CO (except the central one) coincide with dust lanes, which show up dark in the $I-K$ map.

with the bar, apart from at its ends, shows up to the northwest of the center as a string of H II regions. These regions lie just north of the major dust lane seen in optical images. The spiral arm which they outline connects the main disk of the galaxy, through the end of the bar, to the central kiloparsec region, indicating a dynamical connection to the rest of the galaxy. The same pattern can be seen on the southeast side of the bar by following the dust lane, but it shows up less clearly here in Hα.

Dust lanes are visible throughout the disk, but a detailed study of scale lengths through broadband filters (*B*, *V*, *R*, *I*) shows that on average, the optical depth in dust is low, both in the arms and in the interarm zones (Beckman et al. 1995). The corotation radius in the disk has been estimated to be at ~5 kpc, using an ionized gas rotation curve (Arsenault et al. 1988), and at 5 ± 0.5 kpc (Canzian & Allen 1995), following the two-dimensional test for reversal of streaming motions (Canzian 1993) in the Hα velocity field. Sempere et al. (1995), however, find a corotation radius of some 7.3 ± 0.7 kpc, well beyond the ends of the bar, applying a similar test to an H I velocity field, a value in agreement with the results of the morphological determination by Elmegreen, Elmegreen, & Seiden (1989).

In the outer parts of the H I disk, Knapen et al. (1993a) found a deviation in the velocity field accompanied by a faint extension in H I density, most probably as a result of the companion NGC 4322. Its small size and a relatively large separation from the parent galaxy speak against a strongly interacting system NGC 4321/4322. Hence, we neglect the effect of NGC 4322 on the SF and dynamical evolution in the central kiloparsec of NGC 4321.

3.2. *Optical and NIR Morphology of the Central Zone*

Paper I described the most important morphological features in our *K*-band and optical images. Here we summarize this discussion and provide additional details which were left out.

The Hα morphology around the nucleus (Fig. 5) is dominated by four main components (labeled Hα1 to Hα4), first picked out by Pogge (1989), and tentatively identified by Pogge and by Cepa & Beckman (1990) as a four-armed minispiral. Each component is broken up into a number of individual "hot spots" in which strong SF is taking place, and which are also clearly seen in the *U*- and *B*-band images (Fig. 1). Sixteen percent of all the Hα emitted by NGC 4321 comes from this zone of some 30″ diameter, yielding $\sim 3.0 \pm 0.5 \times 10^{40}$ ergs s^{-1}. The nucleus, although clearly detected in Hα, is not particularly strong, and it shows no measured extension. Inside the area bracketed by the four Hα components, a region of reduced Hα intensity is seen (inset Fig. 5), whose isophotes of minimum Hα emission lie along the general direction of the bar.

Two color index images of the circumnuclear region gave characteristic information on stars and dust, respectively. In the $U-I$ image (Fig. 3), darker parts correspond to redder regions in the galaxy, which can be caused by dust extinction, or by a change in stellar population (young stars causing more blue emission). It is not possible to distinguish between these two effects on the basis of a $U-I$ map alone. In the $I-K$ color index map (Fig. 4), there is relatively little change resulting from varying stellar populations between *I* and *K* (Rix & Rieke 1993), but while the effects of dust extinction are low in *K*

($A_K/A_V = 0.11$), they are quite substantial in I ($A_I/A_V = 0.48$). A red (or dark in Fig. 4) zone in the $I-K$ map thus directly indicates the presence of dust there. It reveals a picture of two dust lanes coming in from outside the inner 1 kpc zone along the concave edges of the spiral arms in the disk, swinging in toward the inner barlike region, and continuing further on, practically parallel to the bar major axis. The $U-I$ map defines the detailed locations of SF. In Figure 3, the pattern of four elongated segments mentioned above can be seen clearly, together with the smaller "hot spots" which compose each segment. From the $I-K$ (Fig. 4) and *HST* V-band (Fig. 6) images, it is clear that the inner spiral is in fact two-armed, not four-armed as indicated by the blue and Hα emission, and most clearly delineated by the strong dust lanes running along the arms. The four-segmented appearance is caused by dust lanes crossing the arms, most clearly seen to the southeast at ~8″ from the nucleus, and enhanced SF at specific places along the arms.

In order to study the detailed morphology in the NIR, we determined the run against radius of the azimuthally averaged values of surface brightness (μ, in mag arcsec^{-2}), P.A., and ellipticity (ϵ, defined as $1 - b/a$, where b/a is minor-to-major axis ratio) of the K image ($R < 35''$) and of an I image of the whole disk of the galaxy (used for $10'' < R < 80''$). Ellipses were fitted to the isophotes, making a least-squares fit to the pixels in a selected intensity range in the image. Unwanted pixel values from foreground stars and cosmic rays were removed interactively. In order to check the consistency of the fits, each ellipse was viewed overlain on the original image, with the selected pixels highlighted. In most cases, ellipses were fitted at 0.2 mag arcsec^{-2} spacings. Although the results from the two images can be compared in terms of structural properties of the disk, it must be kept in mind that properties of dust and stellar populations differ from I to K, and that results from the two passbands are not interchangeable. The results are presented in Figure 8, showing the run of the K and I surface brightness, P.A. and ϵ against radius.

The approximate range in radius of the separate components, as named in Paper I, where most of them were morphologically defined from the K image, is indicated in the middle panel of Figure 8. These components are, from inside out: (i) a small *bulge* component ($0'' < R < 2''$; $\epsilon < 0.2$); (ii) the *inner barlike region* ($2'' < R < 4''.5$; P.A. $= 111° \pm 1°$; ϵ slowly rising from 0.2 to 0.5); (iii) two *leading arms* ($4''.5 < R < 7''$–$8''$; ϵ is reaching a maximal value of 0.6 ± 0.04) in a region where the contours in the K image clearly deviate from what is expected from a bar by becoming progressively twisted in the direction of rotation, toward larger P.A. (anticlockwise), i.e., in the leading sense with respect to the bar. This twisting occurs in the region where leading arms are expected theoretically and are modeled numerically by us (§ 5); (iv) two *peaks of emission* (K1 and K2 in Fig. 3) ($R \sim 7''$–$9''$; P.A. of the line joining these peaks is $114° \pm 1°$); (v) the oval *ringlike* zone where the SF armlets are found in the optical and Hα ($10'' < R < 22''$; maximum P.A. $= 159° \pm 3°$ at $R \sim 20''$; minimum $\epsilon = 0.13 \pm 0.02$ near $R = 17''$–$18''$). The K contours in this region twist continuously in the leading direction, are smooth, and show hardly any indication of spiral arms or dust lanes. As we argue below (§ 6), these apparent changes in morphology are caused by population changes, along with the much reduced absorption by dust at 2.2 μm; (vi) the *large-scale stellar bar* ($R > 30''$; P.A. $\approx 107° \pm 3°$ outside $R = 35''$; maximum $\epsilon = 0.52 \pm 0.04$); (vii) the *main disk* component (not shown in Fig. 8; $R > 90''$; P.A. $= 153° \pm 2°$ and ellipticity $\epsilon = 0.13 \pm 0.03$ take the main disk values [Knapen et al. 1993a]).

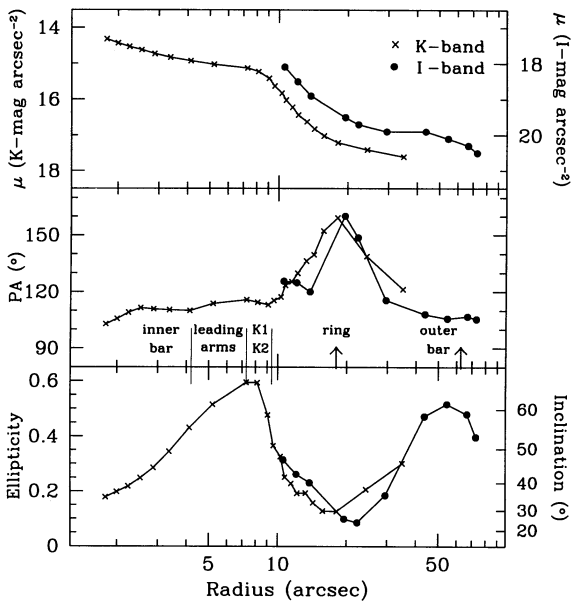

FIG. 8.—Run against radius of three parameters describing the red surface brightness distribution in NGC 4321, as measured from I (*filled dots*) and K (*crosses*) images using ellipse fitting. Values are plotted up to $R = 35''$ as derived from K and for $10'' < R < 75''$ as derived from I. *Top:* surface brightness, in K mag arcsec^{-2} (scale on left side) and I mag arcsec^{-2} (scale on right side). *Middle:* position angle, in degrees, measured N over E. *Bottom:* ellipticity (defined as $1 - b/a$, with b/a the axis ratio). Scale on the right side shows the corresponding angle of inclination, in case the measured ellipticity were solely the result of seeing an intrinsically round object projected on the plane of the sky.

The surface brightness profile shows a relatively steep slope in the region of the ringlike SF zone and a more shallow decrease in the regions of the two bar components (inner and large-scale) surrounding it. In the main disk, the surface brightness shows an exponentially falling profile (see, e.g., Beckman et al. 1995).

The determinations of P.A. and ellipticity indicate that the zone where the SF armlets are seen in Hα ($10'' < R < 22''$) most probably is intrinsically round, and lying in the plane of the main disk. The inner barlike structure and the large-scale bar have the same P.A. and similar ellipticity and are thus aligned to within the errors of the fitting procedure. Both are of roughly the same strength, a further indication that only one stellar bar is present. The gradual skewing of K and I isophotes inside and outside the SF zone so notable in Figure 8, in P.A. and ϵ, is an indication for the presence of ILRs and will prove to be important when we discuss the interplay of dynamical resonances with the gas flow and SF.

The K peaks K1 and K2 are elongated perpendicularly to the bar's major axis, for 2″–3″, along the spiral arm segments seen in Hα (labeled Hα1 and Hα2 in Fig. 5). The strongest Hα peak in the Hα1 complex corresponds in position to K peak K1, whereas the strongest Hα peak in the Hα2 complex is offset from the K2 peak by some 1″.5. The Hα peak coinciding with K1 is at the position where the *HST* image (Fig. 6) and the $I-K$ color index image (Fig. 4) show strong emission surrounded by a dust shell. There is no obvious Hα counterpart centered on the K2 peak, although the Hα2 complex surrounds

K2 and is clearly associated with it. Paper I showed that the *UVK* colors of selected regions, combined with stellar population models, are compatible with a scenario in which the four peaks K1, K2, Hα3, and Hα4 are caused by coeval bursts of SF, but that whereas Hα3 has somewhat less dust than the similar regions Hα4 and K1, light from K2 is much more reddened by dust extinction and/or absorption. We conjecture that K1 and K2 are two similar starbursts, where K1 has already broken through the dust, whereas K2 is still buried in the dust lane.

3.3. *Effects of Dust Extinction at* 2.2 μm

The $I-K$ color image was used to make a first-order correction for presence of localized dust extinction in the K image (Paper I). We concluded that the observed morphology at 2.2 μm is barely influenced by dust. In correcting the K-image, two assumptions have been made, which are discussed explicitly here.

First, we assumed that the $I-K$ color of the stars in the central region ($R < 15''$) is constant. This assumption is not very severe, and it invokes the property that $I-K$ remains remarkably constant for stellar populations older than $\sim 10^8$ yr (see the models of Bressan, Chiosi, & Fagotto 1994). Apart from the most recent bursts of SF, which have lower (bluer) $I-K$ and show up as white patches in Figure 4, we can assume that the intrinsic $I-K$ color in most of the central region of NGC 4321 lies between 1.65 and 2.0. Since ~90% of the pixels in our $I-K$ image take values between 1.7 and 2.5, the extinction $E(I-K)$ here is never more than 0.85 mag, implying that we are in the optically thin regime in I over virtually the whole central area.

Second, we assumed a Galactic extinction law (Rieke & Lebovsky 1985) in deriving A_K from $E(I-K)$. Knapen et al. (1991) and Jansen et al. (1994) verified the applicability of this law in a number of external galaxies, showing in particular that geometrical effects, including the use of a pure screen model with all the dust in front of the stars, leads to only small differences, especially in the red and NIR parts of the spectrum. Since we are interested in an order-of-magnitude estimate of the extinction in K, this assumption is justified. Using the Galactic extinction law, the extreme value of $E(I-K) = 0.85$ would correspond to $A_K = 0.28$ mag, or about one contour in Figure 2, implying that indeed our extinction correction is very small.

The above assumptions lead to a small correction to the K morphology as a result of dust extinction. Paper I showed that such important features as the leading arms and zones K1 and K2 are not artifacts of dust obscuration (in fact, the leading arms seem to be somewhat hidden by dust). An additional argument in favor of only a small dust correction in K is that a patch of extinction in K of, say, 0.5 mag has a corresponding extinction in V of some 2–4 mag, and even larger in U (~3–6 mag). Such values are excluded by the morphology of the individual and color index images (Figs. 1 and 3), as well as by the surface brightness profile of NGC 4321, which is very much within the normal for spirals of its type (e.g., de Jong & van der Kruit 1994). Thus, we feel confident that the morphology as seen in the K-band image is not significantly influenced by localized dust absorption, and that we can use this image as a solid basis for our modeling and interpretation.

3.4. CO

In Figure 7 we show a contour representation of the CO interferometric map of the central region overlain on a gray-scale map of the $I-K$ color index image. The CO traces localized concentrations of molecular hydrogen gas, but owing to the lack of short spacings in the observations, it is not sensitive to structure on a scale larger than 30″, or maybe even 20″ (B. Canzian, private communication). From single-dish observations by Kenney & Young (1988), Cepa et al. (1992), and García-Burillo, Sempere, & Combes (1994) it is known that the CO distribution in this galaxy rises roughly exponentially toward the center, with an additional central component, possibly caused by the bar (Knapen et al. 1995b). We do *not* see the bulk of this more slowly varying emission in the interferometric image presented here, but we can use the latter map to trace concentrations in the molecular gas that may be caused by shocks. At a distance of some 5″–10″, four main concentrations are seen in CO, of which the ones to the north and south of the center are double. Only the largest of these, to the north, seems resolved at the 6.″9 × 4.″4 resolution of the map; the five others (including the one at the center) are most probably unresolved. The appearance of the CO map is generally confirmed by a new BIMA map with higher sensitivity and resolution discussed by Rand (1995), although the smallest of the two peaks to the north is not present, and the peak west is less pronounced in Rand's data. These differences may be caused by differences between the telescope arrays used (Rand 1995).

Comparing the positions of the circumnuclear CO concentrations with the $I-K$ color index map, where dust shows up as darker regions, it is clear that all CO peaks are positioned in regions of high dust extinction, the north and south concentrations lying in the main dust lanes, where strongest shocks are found in our numerical models. The peaks toward the east and west occur at the end of the barlike feature, where gas orbits crowd and shocks are expected (see below). The CO peaks are also closely related to the main Hα peaks, although lying slightly outside in all cases. We infer that the four CO peaks must correspond to strong molecular concentrations, but only better resolved data, preferably probing different transitions or even molecules, plus modeling could reveal to what extent these peak brightness temperatures are caused by heat input from the SF regions, and what is the precise physical relation between these quantities.

4. MODELING

To understand more fully the response of the gas to the underlying gravitational potential of the central region in NGC 4321 and especially the formation of the nuclear ringlike structure and associated features, we have modeled the stellar and gas dynamical processes there by means of three-dimensional numerical simulations using a method described by Heller & Shlosman (1994). Here we repeat only the necessary details and discuss modifications.

The time-dependent gravitational interactions between gas and stars have been calculated using the TREE algorithm (Barnes & Hut 1986; Hernquist 1987). The gas and stars in the disk were evolved by means of a hybrid SPH/N-body code which is a fully Lagrangian scheme. Dynamic gravitational softening and dynamic smoothing in the gas have been implemented, which resulted in approximately the same accuracy in the smoothed quantities everywhere, or, in other words, to a dynamic spatial resolution. The two-component galactic disk was embedded in a spherically symmetric halo plus bulge potential.

4.1. *Initial Conditions and Star Formation*

The following important point influenced our way of modeling: within 2–3 kpc from the rotation axis, the disk cannot be assumed geometrically thin, and hence the gas and stars cannot be studied by invoking planar motions only. This means that a fully three-dimensional potential is needed in order to reconstruct the motion in and above the galactic plane. However, the uncertainties in the density distribution in NGC 4321 do not warrant the solution of the Poisson equation. We also decided against running a spectrum of models performing a parameter search for the gas flow in the frozen stellar background. The reason for this is that the amount of gas expected to accumulate within this region is sufficiently large to strongly modify the stellar dynamics there. Freezing of the stellar disk, therefore, would result in unrealistic models, as it completely ignores the feedback of the gas on the stars (Shlosman & Noguchi 1993). Instead, we have analyzed the gas dynamics in a three-dimensional model sufficiently similar to NGC 4321 but by no means identical. Only gross features which show robust behavior have been studied. We aim at reproducing (i) the offset shocks in the large-scale stellar bar which are delineated by a chain of H II regions and dust lanes; (ii) the nuclear ringlike structure of SF having four distinct maxima; (iii) the skewing of isophotes from the P.A. of the bar to that of the "ring," both inside and outside the "ring" (as seen in Figs. 2 and 8); and (iv) the approximate alignment between the outer and inner bar structures.

An axisymmetric model of a galactic disk was constructed which is dynamically unstable and develops a stellar bar in the process of evolution. Different parameters of this system have been chosen in order to emphasize the major features of the observed rotation curve in the central few kpc (Arsenault et al. 1988; Knapen et al. 1993a), i.e., the steep velocity gradient within the inner $\sim$400 pc followed by a relatively slow growth up to $\sim$8–9 kpc. The initial mass distribution is that of Miyamoto-Nagai (e.g., Miyamoto, Satoh & Ohashi 1980) and consists of three components: bulge, halo, and disk. A set of hydrodynamical equations coupled to the Poisson equation (Miyamoto et al. 1980) has been solved to obtain the three-dimensional gravitational potential, the density, and the velocity dispersion for each component. The parameters of the three models, Q0 (pure stellar), Q1 (stars + gas, no SF), and Q2 (with SF), are given in Table 1. The bulge and the halo are assumed to be frozen, but the disk components, stars and gas, are evolved self-consistently. The halo mass fraction within the circumnuclear region of 2–3 kpc is negligible; however, it does govern the global stability of the disk as well as the size and other relevant parameters of the forming bar. It is, therefore, of prime importance in the model. The units of mass, distance, and time are $[M] = 1.6 \times 10^{11}\ M_\odot$, $[R] = 10$ kpc, and $[\tau] = 3.75 \times 10^7$ yr. The isothermal equation of state is used for the gas with a temperature of 10^4 K, except for the regions of SF which are treated differently (see below). The disk contains 32,768 collisionless particles (stars) and 8192 collisional smoothed particle hydrodynamics (SPH) particles (gas). For the collisionless particles, the gravitational softening is kept constant, $\epsilon_* = 200$ pc, while for the SPH particles the softening length is set equal to the smoothing length with a lower resolution limit of $\epsilon_{\min,\,\mathrm{gas}} = 200$ pc for models without SF. Models with SF do not require any limit on softening. Finally, the gas is introduced at time $\tau = 0$ by replacing some of the stellar particles by the SPH particles within ± 100 pc from the equatorial plane and inside the radius of 10 kpc, with a radial density distribution identical to that of the stars. We require that the gas amounts to 3% of the total mass within 10 kpc.

TABLE 1

MODEL PARAMETERS[a]

Model Components	Mass	Horizontal Scale Height	Vertical Scale Height
Halo	3.041	1.800	1.800
Bulge	0.105	0.045	0.045
Disk	0.991	0.520	0.020

[a] Miyamoto-Nagai model parameters (Miyamoto et al. 1980) used to model the halo, bulge, and disk. Components are defined by their mass, horizontal scale height, and vertical scale height. Units are given in the text.

The phenomenological approach to treat the effects of SF can be summarized as follows (Heller & Shlosman 1994): (i) a gas particle is considered to undergo "star formation" if the gas is Jeans unstable, if it participates in a converging flow, and if the density in the gas exceeds a critical one, typically $\sim 20\ M_\odot\ \mathrm{pc}^{-3}$; (ii) only massive OB-type stars are formed leaving no remnants; (iii) the OB stars affect the gas by means of their line-driven winds, 10^{51} ergs per $\sim 10^6$ yr of main-sequence evolution, and by supernovae (SNs), 10^{51} ergs per $\sim 10^4$ yr. The deposited energy-to-gas "turbulent" motion conversion efficiency is assumed $\xi \sim 0.05$. The rest of the energy is radiated away instantly (isothermal equation of state). Effects of the initial mass function (IMF) are ignored, which is partly justified by observational evidence that nuclear starbursts have an IMF skewed toward massive stars (e.g., Rieke et al. 1980; Wright et al. 1988; Scalo 1990; Rieke et al. 1993).

4.2. *Modeling Evolution*

A stellar bar, extending up to corotation, forms after about one rotation period in the disk in all three models. The steep velocity gradient of the centrally concentrated mass distribution ensures that the bar is short and of moderate strength. It is capable of driving weak spiral arms only, which in the Q0 model disappear quickly as a result of the heating of the stellar "fluid." Since we are not interested in the transient behavior of the system during the bar instability, we omit this from our discussion (see Heller & Shlosman 1994). The stellar component reaches a steady state after several rotations, which is verified by measuring the strength q of the bar defined here as the maximum ratio of the sum of $m = 2$, 4, 6, and 8 Fourier components to $m = 0$. We measure $q \sim 0.4$ for Q0, and $q \sim 0.3$ for Q1 and Q2 models. Q1 shows the largest fluctuations around this value of q. The bar's pattern speed has stabilized at $\Omega_b \sim 2.1$ (for Q0), with a slight decline during the simulation time of 2×10^9 yr. Models with gas have a slightly higher bar pattern speed ($\Omega_b \sim 2.6$ for Q1 and Q2), as noted in Heller & Shlosman (1994). The gas component never reaches a true steady state, although its evolution slows down substantially after the initial transient phase.

The chosen mass distribution leads to four main *linear* resonances: the outer Lindblad resonance (OLR), the corotation resonance (CR), and the two inner Lindblad resonances—the outer ILR (hereafter OILR) and the inner ILR (hereafter IILR). The latter resonances are the most important ones for our discussion, since they are located within the central region, at $r \sim 220$ pc (IILR) and $\sim$1.8 kpc (OILR) for Q0, and slightly closer to each other in Q1 and Q2, at 240 pc and 1.4 kpc, respectively. The CR is at $\sim$4 kpc. Figure 9 shows the inner

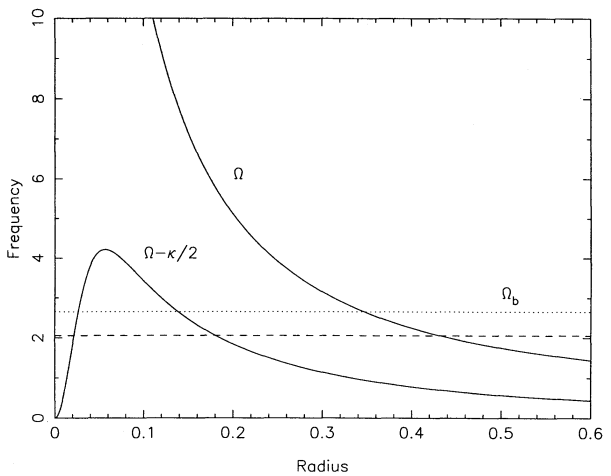

FIG. 9.—Linear resonances for the Q0, Q1, and Q2 models at $\tau = 20$. Horizontal lines correspond to the bar pattern speeds in these models: dashed line for the Q0 model and dotted line for the Q1 and Q2 models.

resonances at the time $\tau = 20$. Note that these numbers are based on the assumption that epicyclic approximation is valid, which means a nearly axisymmetric distribution of material in the disk when the orbits of individual stars are more or less circular. As the bar grows and the amplitude of noncircular motion increases, those results become more erroneous. We use fully nonlinear analysis below to validate the positions of the ILRs.

4.2.1. *Orbit Analysis, Resonances, and Gasdynamics without Star Formation*

In order to understand the specific features of gas flow, we have analyzed the dominant families of periodic orbits in the *NGC 4321–like* gravitational potentials of three numerical models. Our analysis is limited to orbits confined to the equatorial plane. Orbits out of the plane are addressed separately (Heller & Shlosman 1995). This approach was pioneered by Contopoulos & Papayannopoulos (1980), Athanassoula et al. (1983), Pfenniger (1984), and Sparke & Sellwood (1987), among others (see also Sellwood & Wilkinson 1993 for a review). First we provide some theoretical background to the orbit analysis and subsequently discuss the evolution of numerical models. In short, we have symmetrized the gravitational potential in the plane with respect to the bar's major axis and searched for the x_2-type of periodic orbits. These orbits are located between the IILR and OILR and are aligned perpendicularly to the stellar bar. The x_2 orbits exist only between the ILRs and in this way serve as their signature and as extension of linear resonances into the nonlinear domain. The reason for the sharp transition between x_1 and x_2 orbits can be understood within the framework of forced oscillations (e.g., Landau & Lifshitz 1969). Using the epicyclic approximation, it was shown already by Sanders & Huntley (1976) that the response phase of stellar orbits to the bar potential changes abruptly by 90° at each resonance which leads to the appearance of the x_2 orbits between the ILRs and a coexistence of both families in the resonance neighborhood.

While stars can populate different families of orbits within the same region, e.g., between the ILRs, this is not true of gas, which in fact does not experience a true resonance at the ILRs because of the damping term in the linearized equation of radial oscillations (Huntley 1977; Huntley, Sanders, & Roberts 1978; Binney & Tremaine 1987). Instead, a gradual bending of periodic orbits is predicted which leads to the "crowding of orbits" in the neighborhood of the ILRs and to the formation of trailing spiral arms between the CR and the OILR (crossing the OILR), and of leading spirals across the IILR (Sanders & Huntley 1976; Huntley 1977; Huntley et al. 1978). Hence, the gas orbits are aligned with the stellar bar close to the CR and are skewed gradually in the leading direction at smaller radii in the vicinity of the OILR. This phase shift in the gas response should reach a maximum somewhere between the ILRs (close to 90° if the ILRs are separated enough) and then start to decrease. The gas orbits are again aligned with the stellar bar inside the IILR. "Crowding" of streamlines in a highly supersonic ISM flow leads naturally to shocks and the misalignment of gas and stellar responses—to gravitational torques and to the gas inflow within the CR. We note also that the appearance of shocks invalidates the epicyclic approximation for the gas flow and many of its conclusions, e.g., signs of gravitational torques—the gas response is highly nonlinear.

Figures 10*a*–10*b* represent the anatomy of simple periodic orbits in the full gravitational potential of models Q0 and Q1 at time $\tau = 20$ when both gas and stars reached the approximate steady state. Much of the innermost morphology in the models can be understood using these diagrams, although because of shocks and dissipation in the gas these orbits are only remotely related to the gas motion. The main families x_1, x_2, x_3 (prograde), and x_4 (retrograde) are marked. Typical orbits which belong to x_1 and x_2 families are seen in Figure 11 for different Jacobi "energies" E_J, and the domain of x_2 is evident (see Binney & Tremaine 1987 for definition of E_J). The x_2 orbits for the Q1 model are confined to $E_J \approx -5.24$ to -4.21 at $\tau = 20$ and change little with time. Thus, we adopt the above limits as nonlinear ILRs in the E_J space. The corresponding semimajor orbital axes (Figs. 10–11) are ~500 pc and ~1.3 kpc. In comparison with the linear ILRs (Fig. 9), this shows that the region between resonances in the nonlinear regime is reduced for all models.

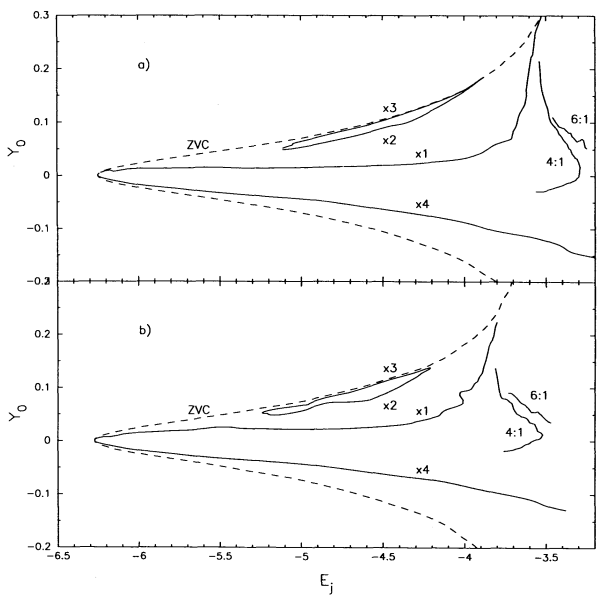

FIG. 10.—Characteristic diagrams of orbit families in the rotating frame of the bar at $\tau = 20$ in (*a*) the Q0 model and (*b*) the Q1 model; y_0 gives the bar minor axis crossing by individual orbits. Dashed line shows the zero velocity curve (ZVC). Only the main families inside 3 kpc are shown.

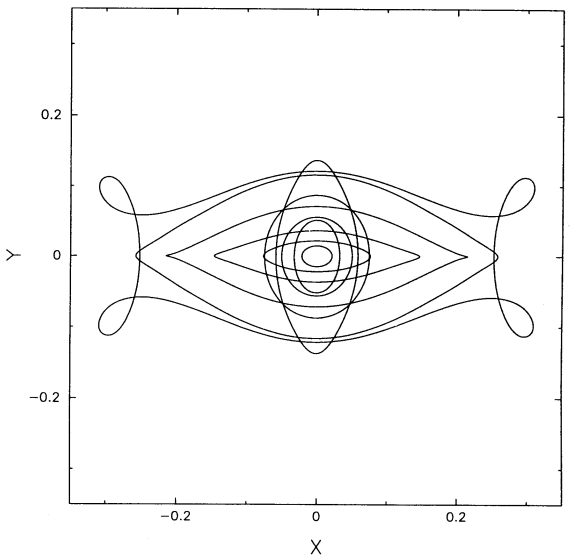

FIG. 11.—A representative set of simple periodic orbits in the gravitational potential of the Q0 model. The stellar bar is elongated along the x-axis. The x_1 family of orbits extends between the OILR and CR and between the center and the IILR. The x_2 family is limited to between the ILRs. Note that the linear analysis (Fig. 9) shows a wider range allowed for x_2.

The responses of stellar and gas components in the models are as follows: in the pure stellar model (Q0), all isodensity contours within the bar are aligned with the bar. This means that although x_2 orbits, as shown in Figure 11, are allowed and the ILRs are present, most of the stars remain on x_1 orbits, a sign that the stellar population in the model is too hot to be trapped. This response is more complex in the presence of gas (model Q1): the gas is losing its angular momentum to the stellar bar between the CR and OILR and falls through toward x_2 orbits as a result of gravitational torques. Some of the gas inside the IILR acquires angular momentum, flows out across this resonance, and settles on the innermost x_2 orbits. Close to the CR, the gas response is parallel to the stellar bar, but further inward the gas is responding with increasing phase shift, producing a pair of offset shocks (Fig. 12). These shocks are curved and concave toward the bar major axis in agreement with two-dimensional numerical simulations of gas flows in analytical bars which have clearly shown that the shock curvature is a function of the bar's strength (e.g., Athanassoula 1992). We note the difference between straight shocks which accompany strong bars and curved shocks, produced in our simulations, more typical of weak and moderate bars. We return to this issue in §§ 4.2.2 and 5.

Between the ILRs, the gas response leads the stellar bar by more than 45°, a phase shift which gradually decreases further inward. The kinematics of this region is clearly dominated by two pairs of shocks: a tightly wound trailing pair (frequently called "nuclear spirals" by observers) discussed above and a leading one which crosses the IILR. Figure 13, at times $\tau = 15$ and 17, illustrates both the formation of the shock system and the intimate relation between shocks. In fact, much of the time one can talk about a single pair of shocks which exhibits a pronounced cuspy feature (caustic) between the ILRs, where the leading arms switch to the trailing ones. So to the extent that these shocks delineate spiral arms, we observe a pseudo-ring made out of a pair of tightly wound spirals between the ILRs. This particular morphology results in the gas accumulating within two elliptical rings between the ILRs as a result of *shock focusing* (Figs. 12–14). The outer ring forms from the shocked gas which flows along the loci of the offset *trailing* shocks crossing the OILR as they curl around the central region. This ring is positioned deep inside the OILR; roughly speaking, the inflowing gas settles on the outer nonintersecting x_2 orbits. The inner ring forms from the shocked gas that flows out along the loci of two *leading* shocks. The major axis of this ring is defined by the cuspy feature described above and extends initially outside the IILR (Figs. 13 and 14*a*–14*b*, e.g., before $\tau \sim 22$). The outer ring develops first, but both grow at approximately the same median rate, $\sim 0.5\ M_\odot\ \mathrm{yr}^{-1}$.

Both rings persist for the duration of the simulation and appear to be initially closely aligned. While the angle between the stellar bar and the outer ring slightly increases with time from ~70°–75° to ~80°–85°, the relative P.A. of the inner ring evolves in the opposite direction. This is illustrated by the orientation of shocks, trailing and leading, in the vicinity of the rings (Fig. 13), the blown-up figures of the rings, and the velocity field there (Figs. 14*a*–14*b*). The accumulation of gas in the rings increases the gravitational torques they experience from the stellar bar. The rings subsequently evolve as to minimize the total torque on the gas, which is the main reason why the outer ring orients itself along the x_2 orbits, more or less, while the inner ring, which shrinks toward the IILR with time, stabilizes along the x_1 family, leading it by less than 10° (Figs. 13 and 14*a*–14*b*; note the abrupt change in the orientation of the outer ring between $\tau \sim 19$–20). After $\tau \sim 20$, the morphology of the central region persists for the rest of the numerical simulation, $\sim 2 \times 10^9$ yr, although the shocks alternate in strength and the continuity between them is not so evident as before. The relative orientations of major dynamical constituents are now similar to those observed in NGC 4321. In particular, there are two density enhancements in the resonance region which are located where the large-scale offset shocks and the flow alongside join the outer ring, i.e., in the neighborhood of the bar minor axis and downstream from there. An additional pair of density enhancements is associated with the leading shocks in the inner ring which culminate at the apocenters of the flow in the same region, lying slightly ahead of the bar's major axis. Both are depicted in Figures 13 and 14*a*–14*b* and correspond to the loci of SF and peaks of the CO distribution in the region, as discussed below. We emphasize that because the inner ring is roughly elliptical, there is a substantial flow slowdown and gas accumulation at the apocenters of circulation within the ring.

Although the rings corotate with the stellar bar throughout these simulations, they represent only a *temporary slowdown* of the gas inflow. The outer ring "leaks" the gas onto the inner ring which contains orbits deeper in the potential well. Since the inflowing gas rotates faster than the inner ring, it shocks continuously against the rear of the ring, reinforcing the leading shocks there. Becoming more massive, the inner ring shrinks across the IILR ($\tau \gtrsim 22$) and further inward. At the late stages of evolution, the inner ring becomes increasingly gravitationally unstable to fragmentation because of a high surface density (Toomre 1964; Goldreich & Lynden-Bell 1965). However, this evolution may already be affected by the limiting gravitational softening adopted. About a third of the total amount of gas in the disk has been accumulated in the rings by the end of numerical simulation, $\sim 6 \times 10^8\ M_\odot$ in the inner and $\sim 10^9\ M_\odot$ in the outer ring.

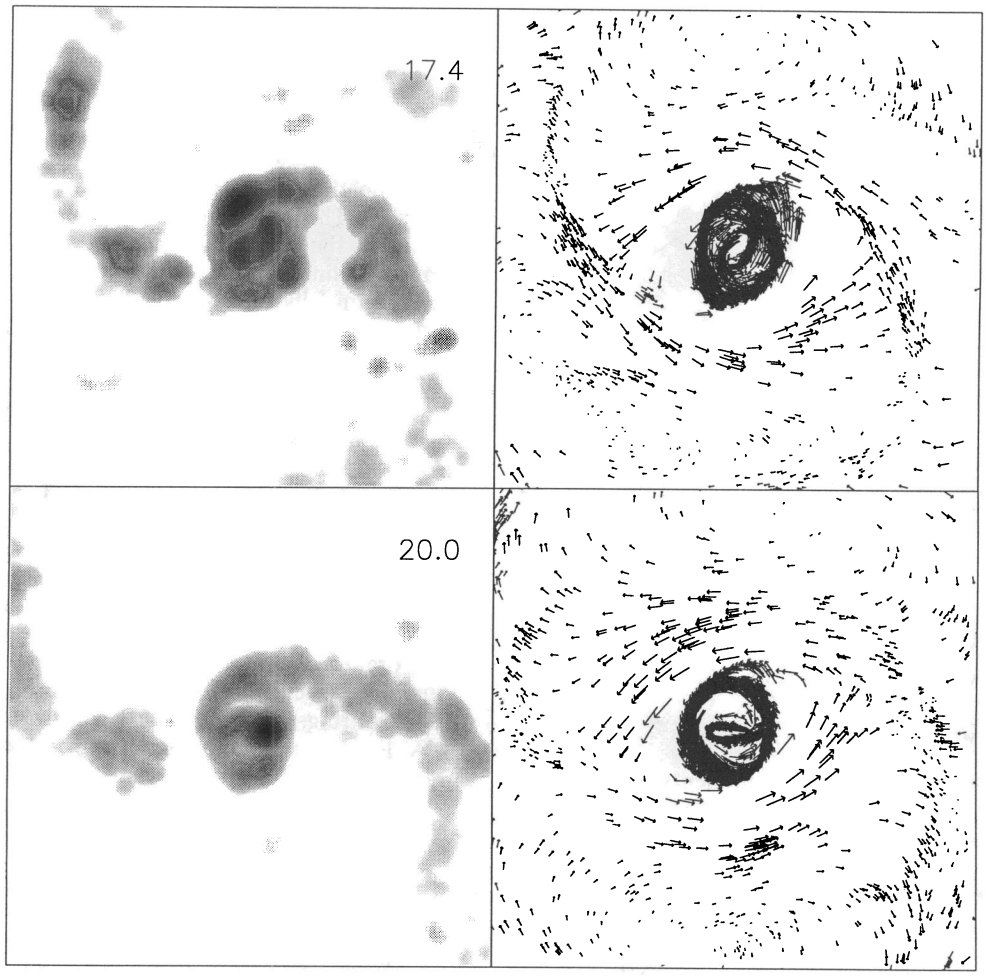

FIG. 12.—*Left:* Logarithmic gray-scale map of shock dissipation in the Q1 model emphasizing the large-scale offset shocks between the CR and the OILR at $\tau = 17.4$ (ring formation) and $\tau = 20.0$ (steady state). Each frame is 8 kpc across. The gray level is given by the time derivative of the nonadiabatic component of internal energy. The rings are "overexposed." The gas flow is anticlockwise, and the stellar bar is horizontal. *Right:* Gas flow in the bar's frame of reference which corresponds to the shock pattern on the left. Vector size is scaled with the velocity. Only half the particles are shown. Note the blobby character of dissipation in the gas. The sharp break in the spiral arms occurs approximately at CR ($\tau = 20$).

4.2.2. *Effects of Star Formation in the Resonance Region*

Owing to many uncertainties in our treatment of SF, the results of this section should be viewed as qualitative. Technically, SF is introducing "turbulent" motion into gas (see § 4.1) and induces mixing between gas with different angular momentum. This effect is best seen in the ring evolution between the ILRs (model Q2). Rings widen and share a large fraction of the material. At a later time, they can be considered merged for all practical purposes, and we shall refer to the gas distribution within the OILR as a disk. Although the "hole" in the gas distribution within what was an inner ring in the Q1 model is now closed, the outer boundary of this disk is well defined and related to the outermost x_2 orbit. It has a slightly oval shape and is positioned almost at right angles to the stellar bar (as in the Q1 model).

Throughout this paper we have been emphasizing the close relationship between the shocks and the SF within CR. Model Q2 (Fig. 15) illustrates this dependence by showing the shock system and SF within the central region of 1.3 kpc. Not all the regions of shocked gas are gravitationally unstable, as the comparison between the shock and SF maps show. The SF is clearly delineating two usually elongated regions where the inflow along the outer shocks encounters the gas between the ILRs. In addition, a double peak dominates the SF in the neighborhood of the IILR, at the position of the cuspy feature, lying slightly ahead of the stellar bar's major axis, as discussed earlier (Figs. 13 and 14*a*–14*b*), where the gas flow is reaching its apocenter of circulation (see § 4.2.1). All four regions of intense SF correspond to the maxima of dissipation in the gas of the Q1 and Q2 models. The two SF regions on the bar's major axis also show gas accumulation as a result of their being the apocenters of the gas flow in the inner "ring." Large surface density in the gas and velocity minima lead to Jeans instability here. Furthermore, a certain degree of SF asymmetry is seen in the SF map (Fig. 15) of the central region in accordance with the Hα observations described in Paper I. A simple explanation for this effect is that although the SF in the model is driven by a bar-induced density wave, Jeans instability is a local phenomenon affected by the clumpiness in the gas. This introduces a degree of stochasticity to the distribution of Jeans-unstable regions along the wave.

The flow pattern is strongly perturbed in the vicinity of SF as a result of the locally induced "turbulence," but it reforms

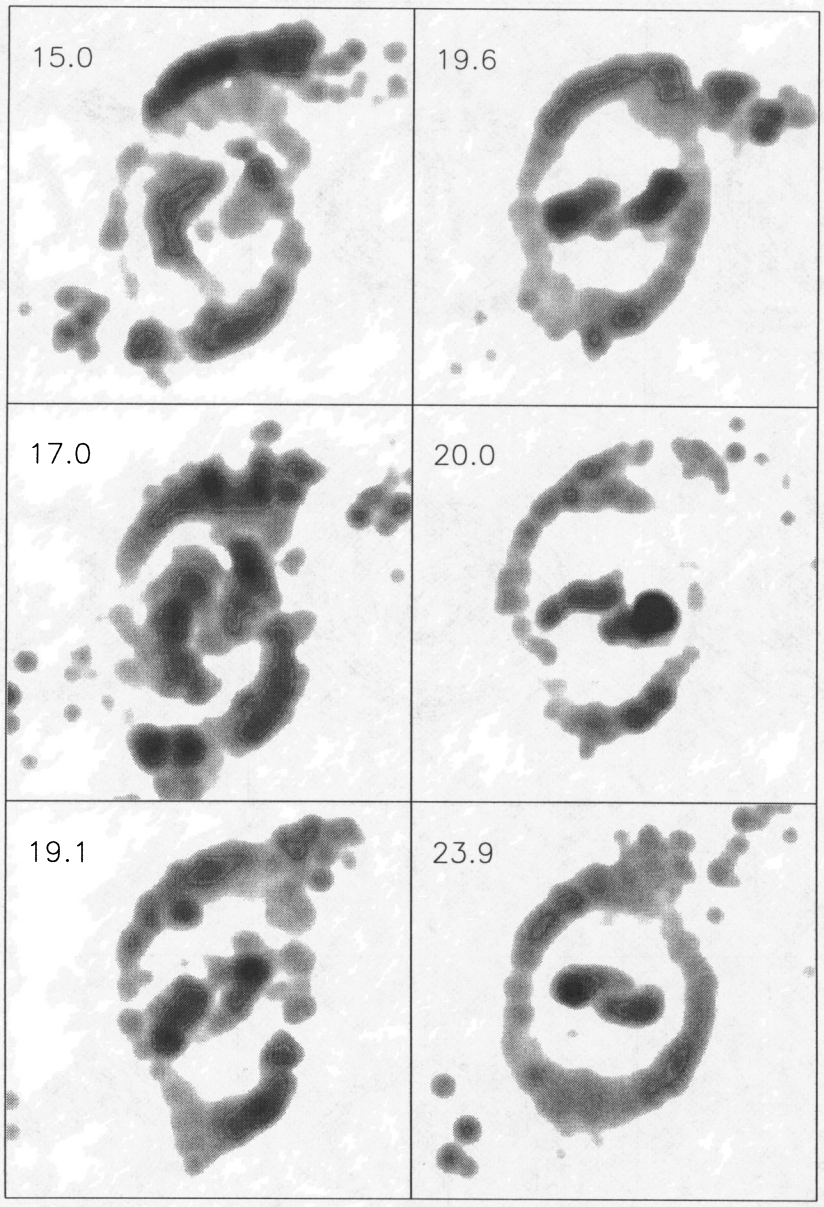

FIG. 13.—Logarithmic gray-scale map of shock dissipation in the Q1 model emphasizing the evolution of shocks inside the OILR. Time is given in the upper left corners. Each frame is 2.6 kpc across. The gray level is given by the viscous dissipation rate. The gas flow is anticlockwise, and the stellar bar is horizontal.

again and again. Hence, the prevailing morphology inferred from the Hα imaging is reproduced and shows a robust behavior. Only at the latest stage of the numerical simulations, as we discuss below, does this picture change as a result of the overwhelming effect of energy deposition by the massive stars which substantially modify the nature of the gas circulation at the center. The SF between the ILRs, i.e., between 0.5–1.3 kpc, reaches the peak rate at $\tau \sim 24$–28. Its amplitude is variable to within a factor of ~ 3, exhibiting a burst behavior with a typical timescale of $\sim 10^7$ yr, similar to that found by Heller & Shlosman (1994) and which is caused by the ability of massive stars to destroy the flow pattern when a sufficient number of them coexist in a particular place.

The evolution of Q1 and Q2 models bifurcates after $\tau \sim 28$ ($\sim 2 \times 10^9$ yr): in Q2, the mass inflow rate across the IILR peaks up strongly, almost tenfold, practically resulting in the catastrophic loss of the angular momentum and collapse of interresonance material toward the central 500 pc with the final product being a "fat" and oval disk, as found by Heller & Shlosman (1994). After $\tau \sim 32$, the relative orientation of this disk is almost exactly parallel to the stellar bar, because the gas settles on the x_1 orbits deep within the IILR as a result of gravitational torque from the stellar bar. The SF now is almost exclusively concentrated within the IILR, being peaked at the nucleus, and the overall morphology has little resemblance to that of NGC 4321. Based on this numerical model, we conclude that a characteristic timescale for "filtering" the gas across the inner resonance zone is $\lesssim 10^9$ yr.

1995ApJ...454..623K

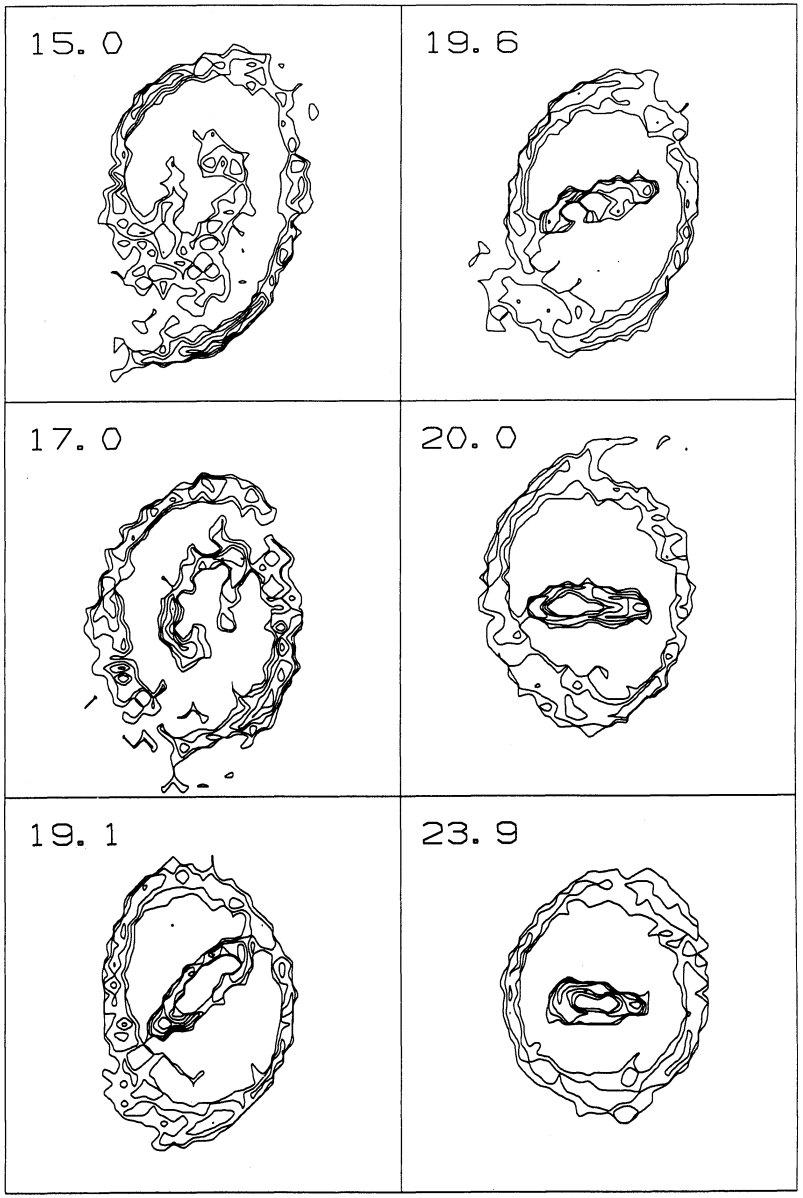

FIG. 14*a*

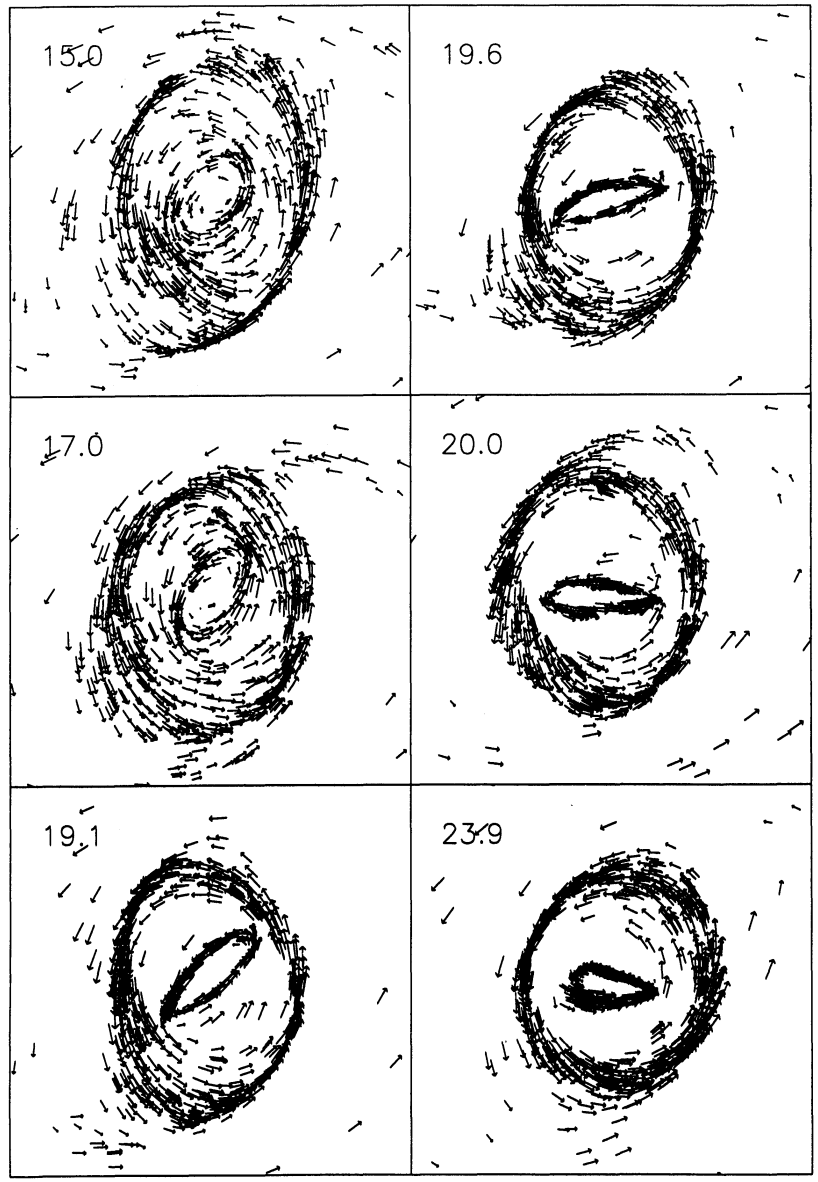

FIG. 14*b*

FIG. 14.—(*a*) Logarithmic gas isodensity contours in the circumnuclear region (Q1 model) shown in Fig. 13. (*b*) Gas flow in the region shown in Figs. 13 and 14*a*, in the bar's frame of reference. Vector size is scaled with the velocity. Only a third of the particles are shown.

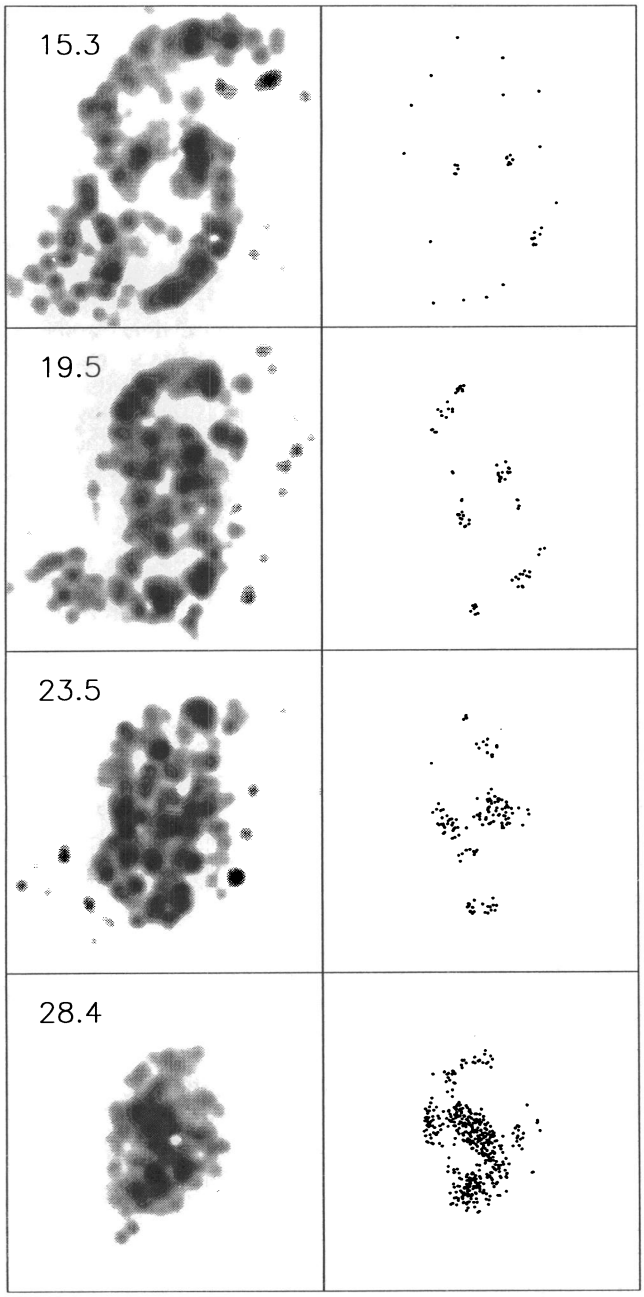

FIG. 15.—*Left:* Logarithmic gray-scale map of shock dissipation in the circumnuclear region (Q2 model). Time is given in the upper left corners. The gas flow is anticlockwise, and the stellar bar is horizontal. Each frame is 2.6 kpc across. *Right:* SF map corresponding to the region shown on the left.

5. DISCUSSION: NIR MORPHOLOGY AND UNDERLYING DYNAMICS

With the new multiwavelength high-resolution data, we are in a position to perform a detailed dynamical study of the gas flow across the nuclear resonance region. Our insight comes from the ability to follow the dust lanes, the exact locations of massive SF, the major concentrations of neutral gas, and the stellar distribution as seen in the NIR, mostly free of the influence of dust extinction (Paper I). Our first and foremost observational result is the confirmation that NGC 4321 is subject to a global density wave driven by a moderately strong and short stellar bar. A number of features observed in NGC 4321 and discussed previously support the resonance character of the circumnuclear region. However, the following two observations are crucial in this respect. First, the strongly offset dust lanes extending from CR inward and delineating shocks in the ISM indicate the presence of two ILRs. This is related to the existence of a family of perpendicular (x_2) orbits (if only one or no ILR is present, these orbits disappear and the dust lanes are centered along the bar's major axis). Second, the *K* isophotes are skewed backward from the P.A. of the "ring" toward the P.A. of the stellar bar, both outside and inside the "ring" (Fig. 8). The fact that we see the *K* isophotes returning to the P.A. of the bar at smaller radii is indicative of the presence of an IILR there. Theoretically, leading spiral arms are expected in the vicinity of the IILR and we believe that our Figures 2 and 8, showing the twisting of *K* isophotes backward to the P.A. of the stellar bar, provide the first direct observational indication that such arms indeed exist in the central kiloparsec of NGC 4321, and that the IILR is resolved in this case (see also Paper I).

The existence of a double ILR in NGC 4321, however, does not shed light on the problem of a single/double stellar bar there. Strictly speaking, the almost perfect match between the P.A.'s of the large bar and the inner barlike structure on a scale of a few hundred pc could be a chance alignment, although the probability for this seems to be extremely low. It is the existence of the leading armlets extending from the ends of the inner "bar" further out that is difficult to explain within the framework of two nested bars rotating with different pattern speeds in the same direction. We see no evidence that NGC 4321 possesses gaseous or stellar "bars within bars," which is a rather short-lived phenomenon and, therefore, a sufficiently rare one (Shlosman et al. 1989; Friedli & Martinet 1993; Combes 1994). Summarizing this indirect observational evidence, together with the results of our numerical modeling, we conclude that NGC 4321 hosts only one stellar bar of 60″ radial size.

The UV, optical, and NIR images provide strikingly different views of the circumstellar region. At optical wavelengths, it is dominated by a pair of well-defined tightly wound spiral arms which extend inward and culminate in the intense bursts of SF. Our *U*, *B*, and Hα images (Figs. 1 and 5) show the prominent sites of SF, somewhat shielded by the dust in its strongest concentrations. The elongated curved arm segments in these images are aligned along the trailing offset shocks seen in dust. It is remarkable that these arms are so tightly wound that they fill up the available space around the inner "bar," and in contrast to arms which form further out in galactic disks, there is not much room for interarm zones, as is clearly seen in the *HST* image (Fig. 6). The Hα arms are parallel to the dust lanes and partially embedded in dust, although at higher *HST* resolution to the bright Hα regions within the arms are seen frequently arranged in chains (spurs) perpendicular to the arms. The strong peaks of SF, Hα1 to Hα4, show up in all young star indicators (see also Paper I). As revealed by numerical simulations, the peaks Hα1 and Hα2 can be associated with the change of character in the spiral arms—from trailing into leading arms. They not only show evidence for young massive stars, but they also coincide with the zones K1 and K2, peaking in the dust lanes which cut through Hα1 and Hα2. The zones Hα3 and Hα4 are strong in OB star indicators (*U*, *B*, and Hα) as well, but they are almost absent in the *K* band, barely

affecting the K isophotes in their neighborhood (Fig. 2). This is further confirmed by the progressive blurring of the arm structure seen in the broadband images with increasing wavelength. In I there is little arm-interarm contrast, and in K it has essentially disappeared (Fig. 1).

Our Figure 3 (and Fig. 4 in Paper I) underline the blue colors of the circumnuclear "ring" of SF regions. This is in apparent contradiction with the red colors inferred by Shaw et al. (1995). The resolution of this puzzle lies in that Shaw et al. misidentify the position of the SF "ring" and in fact measure the colors interior to it, in the inner barlike region.

Of the four key SF zones in the nuclear ring, Hα1 (and K1, its NIR counterpart) is most notable morphologically for its round form in the visible and in $I-K$, where it is seen to be surrounded by a circular dust pattern. This gives a strong impression of an expanding starburst pushing back a dust shell, and it would be interesting to test this with suitable kinematic observations. The Hα2 zone is less prominent: based on comparison with photometric models (Paper I), we believe that it is in an earlier stage of starburst activity than is Hα1 and still hidden in the dust. Its K2 counterpart is reassuringly similar to K1; both lie on a straight line through the nucleus, equidistant from it, and have almost identical morphologies and luminosities in K, all of which supports the above argument. Based on the inferred morphology, we identify both K1 and K2 with the cuspy feature in our numerical simulations. As in the numerical simulations, it is observed slightly to lead the major axis of the stellar bar.

NIR imaging reveals a 60″ radial length, moderate-strength bar, which contributes significantly to the underlying mass distribution and is barely detectable at visible wavelengths. The stellar bar is "dissected" by a region around 1.3 kpc where K isophotes have low, ~0.13, ellipticity and show a maximal departure from the P.A. of the bar (Fig. 8). The curved dust lanes, as seen in the $I-K$ color index image and also on the *HST* image, are indicative of shocks in the gas. They appear strikingly symmetric in $I-K$ (Fig. 4) and seem to be a part of global density wave induced by the stellar bar. Numerical simulations, ours and elsewhere, indicate that weak and moderate bars, which also have a higher probability of possessing ILRs, have curved shocks along the leading edges of the bar accompanied, as is evident from observations, by a string of H II regions (Athanassoula 1992, and references therein). On the other hand, SF seems to be inhibited in straight shocks accompanying strong bars as a result of the large shear in the postshock region (Athanassoula 1992; Heller & Shlosman 1994).

The ringlike structure is clearly formed by a pair of tightly wound spirals which are delineated by dust and a string of the H II regions slightly offset from dust lanes. The Hα intensity rises steeply after the spiral arms cross the bar's minor axis and approach the major axis along the Hα1 and Hα2 arcs. These arms continue further inward for another 180° along the Hα4 and Hα3 arcs, respectively, and terminate at the bar's major axis, at K1 and K2 maxima (Figs. 4 and 6). The Hα intensity then drops again at around 500 pc, which is just *outside* the region of steep velocity gradient. The intensity of CO emission has, apart from the nucleus, four pronounced maxima in the dust lanes penetrating the circumnuclear SF zone. The first two maxima can be found where the dust lanes cross the bar's minor axis (and the ringlike SF region). Two additional maxima are located on the bar's major axis, at the dust lane crossings.

We estimate the total SF rate within the central kpc at ~0.3 $M_\odot$ yr^{-1}, using the Hα luminosity (Kennicutt 1983) although not taking into account the dust obscuration. For a comparison, our numerical simulations provide an inflow rate of ~0.5 $M_\odot$ yr^{-1}, with occasional fluctuations by a factor of ~3–5 around this value. This infall toward the central kiloparsec is clearly driven by the stellar bar. The SN rate in the region can then be inferred at just below 0.01 yr^{-1}, assuming that stars more massive than 5 $M_\odot$ become SNs. Nonthermal radio emission from SN remnants (SNRs) in the circumnuclear "ring" has been detected in 2″ resolution Very Large Array observations by Weiler et al. (1981), who claimed a spectral index ~ −0.8 in the range of 1–23 GHz. The radio map of the central region shows similar morphology to that detected in Hα (compare their Fig. 1 with our Fig. 5) and allows us to obtain an independent estimate for the SN rate in the region, following Ulvestad (1982), at ~0.02 yr^{-1}. Taken at face value, this would mean that the Hα extinction in the starburst zone is around a factor 2–3. Correcting the SF rate in the central kiloparsec for dust obscuration and using the estimated amount of molecular gas there gives a characteristic consumption time of ~6×10^8 yr. At the same time, the SNRs currently dominating the radio emission from the "ring" should be younger than 5×10^7 yr (e.g., Ulvestad 1982). If mass supply to the "ring" is intrinsically intermittent with a characteristic time of a few $\times 10^7$ yr—the local orbital timescale, as hinted by numerical simulations (here and in Heller & Shlosman 1994)—the current population of SNRs may very well be an indicator of the latest burst of SF activity at the center of NGC 4321. A similar timescale has been confirmed for a nuclear starburst galaxy NGC 7552 (Forbes et al. 1994) using population synthesis modeling.

The high-resolution K image presented here is central to our understanding of the inner morphology which, as seen in NIR, is very different from that in visible light, e.g., in the V-band *HST* image or in Hα. This difference is partially caused by the transparency of the ISM at 2.2 μm, where effects of dust extinction on the morphology are greatly reduced ($A_K/A_V = 0.11$). While localized traces of extinction are still present in K (Fig. 2), as evident after correcting for dust extinction (Paper I), we conclude that the morphology is primarily determined by emission.

What is the origin of NIR light in the central region of NGC 4321? In the absence of a strong AGN, the K luminosity in a starburst galaxy comes mainly from (1) the main population of stars, which for a Salpeter IMF means red giants (dominant contribution in quiescent galaxies); and from (2) red supergiants. In addition, about 20%–30% of the K light can be contributed (in extreme cases) by (1) free-free emission from ionized gas; (2) massive blue stars; and (3) very hot $T > 500$ K dust (e.g., Telesco 1993).

The distribution of K light from red giants is expected to follow the overall mass distribution because the number of giants is, under very general assumptions, proportional to the total mass in stars. We have noted before that red and NIR isophotes are aligned with the stellar bar close to CR and inside the circumstellar "ring," while gradually skewed toward the P.A. of the "ring" at intermediate radii. This *gradual* skewing of the P.A.'s of K isophotes is difficult to interpret in terms of an old stellar population, which should be either aligned with the bar (x_1 orbits) or perpendicular to it (x_2 orbits). However, twisting of isophotes can be explained by invoking a nonnegligible contribution from red supergiants,

i.e., from young stars, which trace the gas flow. If sufficient gas is trapped on these orbits, its gravitational attraction may also influence the main stellar population (Shaw et al. 1993), depending on the amplitudes of the stellar dispersion velocities, i.e., the temperature of the stellar "fluid." The newborn stars move away from their places of origin because of azimuthal (phase) mixing and because of heating up in a few orbital times, some 10^8 yr in the present case, while more than 10^9 yr would be needed for the K light to be dominated by the low-mass giants. A 30 $M_\odot$ O star evolves toward the red supergiant phase in a shorter time ($\sim 5 \times 10^6$ yr) and should generally follow the original gas orbits, thus preserving the K isophote twisting. At the same time, the more delicate spiral structure will be largely erased in the NIR.

Supergiants have been found to contribute much of the NIR light in starburst galaxies (e.g., Rieke et al. 1980; Scoville et al. 1988; Forbes et al. 1992; Forbes et al. 1994; Telesco 1994). This trends seems to be present within the center of NGC 4321 as well: after correcting the dynamical mass (obtained from the measured rotation velocities; Arsenault et al. 1988, Knapen et al. 1993a) by the observed mass of molecular gas (from Cepa et al. 1992), the estimated stellar mass-to-K luminosity ratio M_*/L_K is ~ 0.3–0.4 $M_\odot/L_\odot$ inside 1 kpc, compared to $M_*/L_K > 0.7$ $M_\odot/L_\odot$ outside the ring, the latter being typical of a giant-dominated stellar population (Worthey 1994). This indicates that the K emission from the circumstellar region contains a significant fraction of light from a young stellar population, mixed with light from a normal old population characteristic of stellar bars.

Is this consistent with the appearance of the K1/2 peaks in the NIR? If red supergiants are causing the K peaks, they must be dynamically confined for times comparable with $\sim 10^7$ yr which correspond to the evolution of an OB star to the supergiant phase. Otherwise, a star born from a gas moving with a relative velocity of ~ 30 km s^{-1} to the spiral pattern would be found at a distance of ~ 300–400 pc from its birthplace at the time it becomes a red supergiant. This would erase any spiral features as well as the two prominent peaks in K in the central region, unless the latter are gravitationally confined. Hence, K1/2 regions may represent aging starbursts. Numerical simulations described in the previous section show that the gas is slowed down substantially in the vicinity of the cuspy features which we have associated with the K1/2 peaks. Kinematically, the K1 and K2 regions are especially favorable for gas accumulation, for Jeans instabilities in the gas, and for SF (Fig. 15).

Alternatively, young blue massive stars and not red supergiants could dominate the K-band continuum of K1/2 regions with an additional contribution from very hot dust (which is heated directly by stellar radiation) and from the free-free emission in the ionized hydrogen and helium. Within this framework, the K1/2 regions are giant SF complexes triggered and *maintained* by the global gas response to the stirring action of the large stellar bar, which again would explain their remarkable symmetry with respect to the nucleus and the bar itself. Indeed, the existence of some hot massive stars can be inferred directly in K1 through Hα emission, and all four SF regions reveal similar colors in a $U-V$ versus $V-K$ diagram (Paper I).

To estimate the contribution from young massive stars, accompanied by free-free and hot dust emission from their Hα regions, NIR colors are necessary. We note that similar estimates have been performed for e.g., NGC 3310 by Telesco & Gatley (1984), who found that around 10%–20% of NIR emission originates in the blue stars (see also Telesco 1993), and that a comparable contribution from hot dust was invoked for the NIR stellar bar in NGC 1068 and other starbursts (Thronson et al. 1989; Scoville et al. 1988). On the other hand, we discard the possibility that collisionally shock-heated dust can contribute substantially to the K emission in NGC 4321. Telesco, Dressel, & Wolstencroft (1993) argued that collisional heating of dust in SNR shocks is not a viable mechanism to account even for mid-IR emission from a typical starburst, concluding that the dust is primarily heated by light from young massive stars. NGC 4321, being a mild starburst, should fall within this category as well.

All four of the Hα zones are accompanied by prominent peaks in CO emission which are seen superposed on the dust lanes (Fig. 7). The CO peaks also seem to indicate the regions where the shocks are strongest, as revealed by the numerical modeling (Fig. 15*a*). If we correctly understand the kinematics of this region, the bulk of CO emission is located slightly upstream from the corresponding Hα peaks. In galaxies, CO, as a tracer of molecular gas, is usually found close to dust lanes, because the H_2 whose presence stimulates the CO rotational emission is formed catalytically on grain surfaces and is shielded by dust from dissociation by the UV photons. The emission strength in CO depends on both the column density and the temperature of the molecular clouds detected. The peaks in CO are obviously associated with the dust lanes and with the Hα1–4 SF complexes, but we are unable to say whether their location is determined by peaks in the molecular density, maxima of shocks in the neutral gas, the heating of the neutral gas by OB stars, or a combination of these factors. This is an important question which cannot be solved in the present context.

We estimate that H_2 constitutes $\sim 10\%$ of the dynamical mass in the central region, using data from Cepa et al. (1992). Within a factor of 2, this is typical of other circumnuclear starbursts: e.g., NGC 1097 has 7% inside 2 kpc (Gerin, Nakai, & Combes 1988), NGC 3504 has 18% within 1 kpc (Kenney, Carlstrom, & Young 1993); and NGC 3351 has 10% within 500 pc (Devereux, Kenney, & Young 1992). It is not quite clear, however, what the distribution of the molecular gas in the central kiloparsec of NGC 4321 is. The CO map presented here (Fig. 7) is not adequate for this purpose because a significant fraction of the gas at scales larger than 20″ may have escaped the detection in these observations. Although the resolution of 15″ used by Cepa et al. (1992) may just be good enough, the poor sampling in the inner regions make their profile unsuitable as well. García-Burillo et al. (1994) shows a profile along the minor axis of NGC 4321 of CO $J = 2 \rightarrow 1$ observations (their Fig. 2), at 12″ resolution, revealing a central depression. If this depression corresponds to the region inside the SF "ring," the two peaks surrounding it are caused by enhanced CO emission from the "ring," as indicated also by Canzian's data (see Fig. 7). When confirmed, preferably with single-beam data at higher resolution, this molecular gas distribution would be in agreement with our modeling, revealing a concentration of neutral gas in the SF "ring." Examples of other galaxies which host nuclear molecular rings are NGC 1097 (Gerin et al. 1988), NGC 4314 (Combes et al. 1992), and NGC 4736 (Garman & Young 1986); see also Sofue (1991).

Although we have taken the central kiloparsec out of its context in the external framework of the galaxy, it is necessary to refer briefly to this issue. The galactic disk contains two well-defined conventional spiral arms beyond the stellar bar

region, which are observed in H I and CO, as well as in stellar surface density and Hα. These arms are, in fact, connected to the inner spiral structure described here. The Hα image (Fig. 5) shows a clear string of H II regions along the bar (in the NW), linked directly with the exterior spiral arms. An overlay of H II regions on the image of NGC 4321 in the Atlas of Galaxies (Sandage & Bedke 1988) or the more modern real-color image (Peletier 1994) confirms that the Hα emission here originates along a strong dust lane. A similar effect can be observed on the other (southeast) side of the nucleus, although the H II regions are not as conspicuous. The dust lane through the bar, however, is clearly seen also on the southeast side. These dust lanes aligned with massive SF are indicative of a direct coupling between the outer and inner disks. The continuity of the dust lanes was noted by Sandage (1961) and is confirmed by the new data and, supposing they correspond to large-scale galactic shocks in the ISM, by our numerical simulations.

6. CONCLUSIONS

We have obtained a multifaceted view of the circumnuclear region in NGC 4321 using a number of observational techniques and have attempted to model it. We have found interlocking morphology, indicative of the presence of two ILRs, and we have studied their associated dynamical influence on the gas flow within the CR.

Much of the disk in NGC 4321 is subject to the density wave driven by a 60″ radius stellar bar of a moderate strength. The bar can be observed directly only when imaged in the NIR. The *K* isophotes are generally aligned with the bar except for the intermediate region around 18″ from the nucleus, where they take a weakly oval shape oriented at a large angle to the bar and lead its rotation. These isophotes are gradually skewed back toward the bar both inside and outside the K "ring." This particular behavior of the NIR isophotes prompted us to assume and test the hypothesis that the central region is host to a double ILR and study the evolution of gas distribution in the gravitational potential of a NGC 4321–like mass distribution, including the SF and its dynamical effects on the gas. We aimed at reproducing the basic morphology within the CR.

The modeling exercise presented here has provided an insight into the stellar and gas dynamics in the barred region of NGC 4321. We have shown that the present morphology there can be explained within the context of gas response to the nonaxisymmetric bar potential and to the underlying mass distribution inferred for this galaxy. Our *nonlinear* orbit analysis confirmed that a double ILR is associated with this mass distribution and that the x_2 family of orbits oriented along the minor axis of the bar exists between the ILRs. We have used the radial extent of x_2 orbits to define the width of the resonance region which narrowed it compared to the one inferred from the galactic rotation curve.

Given that the offset dust lanes within the stellar bar represent large-scale shocks in the ISM, we have been able to model their formation and evolution for a characteristic time of ~ 10 rotation periods, $\sim 2 \times 10^9$ yr. Neglecting the initial transient, the central morphology appears to be robust, showing four main compression zones, namely, two close to the minor axis of the bar (may be associated with the so-called twin peaks), around 1 kpc from the nucleus, where the inward gas flow curls around the circumnuclear region, and two additional compression zones related to the pair of leading shocks which culminate close to the bar's major axis (slightly ahead of it) at the apocenters of gas circulation within the IILR. This is also the region where large-scale trailing shocks turn into leading shocks, creating a pair of cuspy features which serve as loci of SF, as was shown explicitly in the model. Kinematically, they correspond to the minima in the velocity field and are Jeans unstable. We identify the latter compression regions with the K1 and K2 starburst zones in the neighborhood of the IILR at ~ 500 pc from the center. We also note that the location of the OILR is not characterized by intense SF or gas compression, which are located much further downstream. Rather, the OILR can be distinguished on the basis of gas kinematics. Based on our orbit analysis, the OILR should be located outside the SF zone, at around 1.3 kpc from the center. This means that most of the SF in the resonance region happens deep inside and close to its inner boundary at the IILR.

We have no evidence that NGC 4321 possesses two separate stellar bars. Based on our NIR surface photometry, the position angles for the outer and inner "bars" are identical to within the error of determination, and they have similar strength. Taken together with the results of our numerical simulations, this leads us to conclude that only one bar exists in this galaxy. Furthermore, we argued that the overall morphology in the NIR is indicative of the presence of young massive stars within the bar in addition to the normal old population. The gradient of M/L_K across the SF "ring" can be explained by invoking photospheric emission from OB stars, as well as free-free and very hot dust emission. At the same time, the twisting of isophotes in the vicinity of the resonance region requires a population of stars which is dynamically young, i.e., that follows gas orbits (see also Paper I). We find that red supergiants aged less than a few $\times 10^7$ yr are the best candidates, which should be verified by future spectroscopical analysis.

NGC 4321 displays a sharp decrease in SF rate within the central 500 pc. The ovally shaped inner boundary of SF region corresponding to the incoming pair of tightly wound spirals is positioned just outside the steep velocity gradient zone, around 500 pc, where we expect the IILR. We find that the gas experiences a positive gravitational torque from the bar and moves out, flattening the gas distribution there.

NGC 4321 was selected for this study because it displays a nuclear starburst, but it does so in sufficient moderation as not to destroy the evidence for this process by excessively violent circumnuclear activity. It is fair to point out that the actual flows, at least on the scales examined in this paper, so far have not been observed directly. Previously, however, Knapen et al. (1993a) did detect the flow around the bar in H I, with noncircular velocities of tens of km s^{-1}. This gives us prima facie backing for the claim that similar morphology on the smaller scale will lead to similar dynamics and kinematics. Evidently, the flow pattern within the central 1–2 kpc is far more complex than expected, since it involves the flow across the resonance region. The necessary observations to try to detect the flows are currently feasible on $\sim 1''$ scales in the Hα using two-dimensional spectra line imaging techniques. Although it is not yet possible to carry out the same kinds of observations in H I, since the column densities are too low to permit the required observations on 2″–3″ scale with the VLA, one may be able to detect the gas flows in the molecular component, if this can be observed at the required resolution with a mm interferometer.

The numerical modeling of the inner region in NGC 4321 is complementary to the high-resolution multifrequency observations. It underlines certain aspects of gas and stellar dynamics

whose understanding is crucial for explaining the prevailing morphology and the distribution of SF regions. Overall, it exposes the link between the large-scale structure of the host galaxy and its central activity. Of course, the numerical results should be approached with caution, especially the inflow rates and the treatment of SF. Throughout this paper, we have emphasized only qualitative similarities between the observations and modeling. Although we have successfully modeled the main features of the circumnuclear region, we have no proof that our solution is unique. The bulge used is probably slightly too massive and, therefore, the bar's pattern speed is higher than that found by Elmegreen et al. (1989) and Sempere et al. (1995). With all this, we find that the evolution of gas in the vicinity of the ILRs is more complex than described by Schwarz (1984), who used an ad hoc restitution parameter to follow the dissipative collisions between finite size "clouds." Therefore, we feel that NGC 4321 has served as a useful modeling paradigm, and that the techniques employed here can be developed for further use with individual objects. Our approach offers a set of kinematically testable results. Given the kind of initial observational input we have had (the morphology both in the visible and in the NIR, the mass distribution from the rotation curve, and the locations of SF complexes), the model predicts the directions, locations, and approximate magnitudes of the gas flows and shock pattern within the circumnuclear region. Thus, for NGC 4321, but also for other objects, observers using CO interferometers, two-dimensional optical emission-line spectrometers, and the VLA will be able to compare predictions with observations. Interpretation of such observations will never be trivial, if only because of projection effects, but also as a result of the ability of starbursts to erase the conditions which led to their occurrence in the first place.

We thank Moshe Elitzur, Bruce Elmegreen, Juhan Frank, Robert Sanders, and Tom Troland for helpful discussions, and Blaise Canzian for sending us his CO data of NGC 4321 and for his help in using them here. We acknowledge Reynier Peletier for observing NGC 4321 in *K* for us and for numerous discussions. The WHT is operated on the island of La Palma by the RGO in the Spanish Observatorio del Roque de los Muchachos of the IAC. The UKIRT is operated by the Royal Observatory in Edinburgh on behalf of the SERC. This paper is based on observations made with the NASA/ESA *HST*, obtained from the data archives at the STScI, which is operated by the AURA under NASA contract NAS 5-26555. J. H. K. and J. E. B. are partially supported by the Spanish DGI-CYT grant PB91-0510. I. S. acknowledges support from the Gauss Foundation and the IAC (through project P3/86) and thanks Klaus Fricke and John Beckman for hospitality. I. S. also acknowledges NASA grant NAGW-3839 and continuing support from the University of Kentucky Center for Computational Studies.

REFERENCES

Adams, T. F. 1977, ApJS, 33, 19
Arsenault, R., Boulesteix, J., Georgelin, Y., & Roy, J.-R. 1988, A&A, 200, 29
Athanassoula, E. 1992, MNRAS, 259, 345
———. 1994, in Mass-Transfer Induced Activity in Galaxies, ed. I. Shlosman (Cambridge: Cambridge Univ. Press), 143
Athanassoula, E., Bienaymé, O., Martinet, L., & Pfenniger, D. 1983, A&A, 127, 349
Balzano, V. A. 1983, ApJ, 268, 602
Barnes, J., & Hut, P. 1986, Nature, 324, 446
Beckman, J. E., Peletier, R. F., Knapen, J. H., Gentet, L., & Maté, M. J. 1995, in Opacity of Spiral Discs, ed. J. Davies (Dordrecht: Kluwer), in press
Begelman, M. C., Blandford, R. D., & Rees, M. J. 1984, Rev. Mod. Phys., 56, 255
Binney, J., & Tremaine, S. 1987, Galactic Dynamics (Princeton: Princeton Univ. Press)
Blandford, R. D., & Payne, D. G. 1982, MNRAS, 199, 883
Block, D. L., Bertin, G., Grosbøl, P., Moorwood, A. F. M., & Peletier, R. F. 1994, A&A, 288, 365
Bosma, A. 1981, AJ, 80, 1825
Bressan, A., Chiosi, C., & Fagotto, F. 1994, ApJS, 94, 63
Buta, R., 1986a, ApJS, 61, 609
———. 1986b, ApJS, 61, 631
Buta, R., & Crocker, D. A. 1993, AJ, 105, 1344
Canzian, B. 1990, Ph.D. thesis, California Institute of Technology
———. 1993, ApJ, 414, 487
Canzian, B., & Allen, R. J. 1995, in preparation
Cepa, J., & Beckman, J. E. 1990, A&AS, 83, 211
Cepa, J., Beckman, J. E., Knapen, J. H., Nakai, N., & Kuno, N. 1992, AJ, 103, 429
Combes, F. 1994, in Mass-Transfer Induced Activity in Galaxies, ed. I. Shlosman (Cambridge: Cambridge Univ. Press), 170
Combes, F., & Gerin, A. 1985, A&A, 150, 327
Combes, F., Gerin, M., Nakai, N., Kawabe, R., & Shaw, M. A. 1992, A&A, 259, L27
Contopoulos, G., & Papayannopoulos, Th. 1980, A&A, 92, 33
de Jong, R. S., & van der Kruit, P. C. 1994, A&AS, 106, 451
de Vaucouleurs, G. 1963, ApJS, 8, 31
———. 1984, in The Virgo Cluster, ed. O. G. Richter & B. Binggeli (Garching: ESO), 413
de Vaucouleurs, G., de Vaucouleurs, A., & Corwin, H. G., Jr. 1976, Second Reference Catalogue of Bright Galaxies (Austin: Univ. Texas Press) (RC2)
Devereux, N. A. 1987, ApJ, 323, 91
Devereux, N. A., Kenney, J. D. P., & Young, J. S. 1992, AJ, 103, 784
Dressel, L. L., & Gallagher, J. S. 1994, in Mass-Transfer Induced Activity in Galaxies, ed. I. Shlosman (Cambridge: Cambridge Univ. Press), 165
Elmegreen, B. G. 1994, ApJ, 425, L73
Elmegreen, B. G., Elmegreen, D. M., & Seiden, P. E. 1989, ApJ, 343, 602
Elmegreen, D. M., & Elmegreen, B. G. 1984, ApJS, 54, 127
Emmering, R. T., Blandford, R. D., & Shlosman, I. 1992, ApJ, 385, 460
Forbes, D. A., Norris, R. P., Williger, G. M., & Smith, R. C. 1994, AJ, 107, 984
Forbes, D. A., Ward, M. J., DePoy, D. L., Boisson, C., & Smith, M. 1992, MNRAS, 254, 509
Freedman, W., et al. 1994, Nature, 371, 757
Friedli, D., & Benz, W. 1993, A&A, 268, 65
Friedli, D., & Martinet, L. 1993, A&A, 277, 27
García-Burillo, S., Sempere, M. J., & Combes, F. 1994, A&A, 287, 419
Garman, L. E., & Young, J. S. 1986, A&A, 154, 8
Gerin, M., Nakai, N., & Combes, F. 1988, A&A, 203, 44
Goldreich, P., & Lynden-Bell, D. 1965, MNRAS, 130, 97
Hackwell, J. A., & Schweizer, F. 1983, ApJ, 265, 643
Heckman, T. M. 1990, in IAU Coll. 124, Paired & Interacting Galaxies, ed. J. W. Sulentic et al. (NASA CP-3098), 359
Heller, C. H., & Shlosman, I. 1994, ApJ, 424, 84
———. 1995, ApJ, submitted
Hernquist, L. 1987, ApJS, 64, 715
Hummel, E. 1981, A&A, 93, 93
Huntley, J. M. 1977, Ph.D. thesis, Univ. Virginia
———. 1980, ApJ, 238, 524
Huntley, J. M., Sanders, R. H., & Roberts, W. W., Jr. 1978, ApJ, 221, 521
Ishizuki, S., Kawabe, R., Ishiguro, M., Okumura, K. S., Kasuga, T., Chikada, Y., & Takashi, K. 1990, Nature, 334, 224
Jansen, R. A., Knapen, J. H., Beckman, J. E., Peletier, R. F., & Hes, R. 1994, MNRAS, 270, 373
Kenney, J. D. P., Carlstrom, J. E., & Young, J. S. 1993, ApJ, 418, 687
Kenney, J. D. P., Wilson, C. D., Scoville, N. Z., Devereux, N. A., & Young, J. S. 1992, ApJ, 395, L79
Kenney, J. D. P., & Young, J. S. 1988, ApJS, 66, 261
Kennicutt, R. C. 1983, ApJ, 272, 54
———. 1994, in Mass-Transfer Induced Activity in Galaxies, ed. I. Shlosman (Cambridge: Cambridge Univ. Press), 131
Kennicutt, R. C., Keel, W. C., & Blaha, C. A. 1989, AJ, 97, 1022
Knapen, J. H., Arnth-Jensen, N., Cepa, J., & Beckman, J. E. 1993b, AJ, 106, 56
Knapen, J. H., Beckman, J. E., Cepa, J., & Nakai, N. 1995b, A&A, submitted
Knapen, J. H., Beckman, J. E., Cepa, J., van der Hulst, J. M., & Rand, R. J. 1992, ApJ, 385, L37
Knapen, J. H., Beckman, J. E., Shlosman, I., Peletier, R. F., Heller, C. H., & de Jong, R. S. 1995a, ApJ, 443, L73 (Paper I)
Knapen, J. H., Cepa, J., Beckman, J. E., del Rio, M. S., & Pedlar, A. 1993a, ApJ, 416, 563
Knapen, J. H., Hes, R., Beckman, J. E., & Peletier, R. F. 1991, A&A, 241, 42
Kormendy, J. 1982, in Morphology & Dynamics of Galaxies, ed. L. Martinet & M. Mayor (Sauverny: Geneva Observatory), 115
———. 1993, in IAU Symp. 153, Galactic Bulges, ed. H. Dejonghe & H. Habing (Dordrecht: Kluwer), 209

Landau, L. D., & Lifshitz, E. M. 1969, Mechanics (New York: Pergamon Press)
Landolt, A. U. 1983, AJ, 88, 439
Lo, K. Y., Cheung, C. R., Phillips, T. G., Scott, S. L., & Woody, D. P. 1987, ApJ, 312, 574
Martin, P., & Roy, J.-R. 1994, ApJ, 424, 599
Meixner, M., Blitz, L., Puchalsky, R., Wright, M., & Heckman, T. 1990, ApJ, 354, 158
Miyamoto, M., Satoh, C., & Ohashi, M. 1980, Ap&SS, 67, 147
Moles, M., Márquez, I., & Pérez, E. 1995, ApJ, 438, 604
Morgan, W. W. 1958, PASP, 70, 364
Nakai, N., Hayashi, M., Handa, T., Sosue, Y., Hasegawa, T., & Sasaki, M. 1987, PASJ, 39, 685
Norman, C. A., & Silk, J. 1983, ApJ, 266, 502
Peletier, R. F. 1994, Spectrum, 3, 28
Petetier, R. F., & Willner, S. P. 1991, ApJ, 382, 382
Pfenniger, D. 1984, A&A, 134, 373
Pfenniger, D., & Norman, C. A. 1990, ApJ, 363, 391
Pierce, M. J. 1986, AJ, 92, 285
Pogge, R. W. 1989, ApJS, 71, 433
Prendergast, K. H. 1962, in Distribution & Motion of ISM in Galaxies, ed. L. Woltjer (New York: Benjamin), 217
Puxley, P. J., Hawarden, T. G., & Mountain, C. M. 1988, MNRAS, 231, 465
Rand, R. J. 1995, AJ, 109, 2444
Rieke, G. H., & Lebofsky, M. J. 1985, ApJ, 288, 618
Rieke, G. H., Lebofsky, M. J., Thompson, R. I., Low, F. J., & Tokunaga, A. T. 1980, ApJ, 238, 24
Rieke, G. H., Loken, K., Rieke, M. J., & Tamblyn, P. 1993, ApJ, 412, 99
Rix, H.-W., & Rieke, M. J. 1993, ApJ, 418, 123
Sandage, A. 1961, The Hubble Atlas of Galaxies (Washington: Carnegie Inst. of Washington)
Sandage, A., & Bedke, J. 1988, Atlas of Galaxies (Washinton, DC: NASA)
Sanders, R. H., & Huntley, J. M. 1976, ApJ, 209, 53
Scao, J. M. 1990, in Windows on Galaxies, ed. G. Fabbiano et al. (Dordrecht: Kluwer), 125
Schwarz, M. P. 1984, MNRAS, 209, 93
Scoville, N. Z., Hibbard, J. E., Yun, M. S., & van Gorkom, J. H. 1994, in Mass-Transfer Induced Activity in Galaxies, ed. I. Shlosman (Cambridge: Cambridge Univ. Press), 191
Scoville, N. Z., Matthews, K., Carico, D. P., & Sanders, D. B. 1988, ApJ, 327, L61
Sellwood, J. A., & Wilkinson, A. 1993, Rep. Prog. Phys., 56, 173
Sempere, M. J., García-Burillo, S., Combes, F., & Knapen, J. H. 1995, A&A, 246, 45
Sérsic, J. L., & Pastoriza, M. 1967, PASP, 79, 152
Shaw, M. A., Axon, D., Probst, R., & Gatley, I. 1995, MNRAS, 274, 369
Shaw, M. A., Combes, F., Axon, D. J., & Wright, G. S. 1993, A&A, 273, 31
Shlosman, I., Begelman, M. C., & Frank, J. 1990, Nature, 345, 679
Shlosman, I., Frank, J., & Begelman, M. C. 1988, in IAU Coll. 134, Active Galactic Nuclei, ed. D. Osterbrock & J. Miller (Dordrecht: Kluwer), 462
———. 1989, Nature, 338, 45
Shlosman, I., & Noguchi, M. 1993, ApJ, 414, 474
Simkin, S. M., Su, H. J., & Schwarz, M. P. 1980, ApJ, 237, 404
Sofue, Y. 1991, PASJ, 43, 671
Sparke, L. S., & Sellwood, J. A. 1987, MNRAS, 227, 653
Taniguchi, Y., Kameya, O., Nakai, N., & Kawara, K. 1990, ApJ, 358, 132
Telesco, C. M. 1988, ARA&A, 26, 343
———. 1994, Infrared Astronomy (Cambridge: Cambridge Univ. Press)
Telesco, C. M., Campins, H., Joy, M., Dietz, K., & Decher, R. 1991, ApJ, 369, 135
Telesco, C. M., & Decher, R. 1988, ApJ, 334, 573
Telesco, C. M., Dressel, L. L., & Wolstencroft, R. D. 1993, ApJ, 414, 120
Telesco, C. M., & Gatley, I. 1984, ApJ, 284, 557
Thronson, H. A., et al. 1989, ApJ, 343, 158
Toomre, A. 1964, ApJ, 139, 1217
Ulvestad, J. S. 1982, ApJ, 259, 96
Wang, Z., Scoville, N. Z., & Sanders, D. B. 1991, ApJ, 368, 112
Weiler, K. W., van der Hulst, J. M., Sramek, R. A., & Panagia, N. 1981, ApJ, 243, L161
Worthey, G. 1994, ApJS, 95, 107
Wright, G. S., Joseph, R. D., Robertson, N. A., James, P. A., & Meikle, W. P. S. 1988, MNRAS, 233, 1
Young, J. S., Xie, S., Kenney, J. D. P., & Rice, W. L. 1989, ApJS, 70, 699
Zaritsky, D., Rix, H.-W., & Rieke, M. J. 1993, Nature, 364, 313